Computers and Structures 270 (2022) 106854

Contents lists available at ScienceDirect

Computers and Structures

journal homepage: www.elsevier.com/locate/compstruc

# Stability analysis of plates using cut Bogner-Fox-Schmit elements

S. Eisenträger [a], J. Kiendl [b], G. Michaloudis [b], R. Duy [c], Y. Vetyukov [c,*]

[a] University of New South Wales, School of Civil and Environmental Engineering, Sydney, Australia
[b] University of the Bundeswehr Munich, Institute of Engineering Mechanics and Structural Analysis, Munich, Germany
[c] TU Wien, Institute of Mechanics and Mechatronics, Vienna, Austria

ARTICLE INFO

*Article history:*
Received 11 January 2022
Accepted 15 June 2022
Available online 27 June 2022

*Keywords:*
Stability analysis
Bogner-Fox-Schmit elements
Finite cell method
Kirchhoff plate theory
Isogeometric analysis

ABSTRACT

In this paper, the classical $C^1$-continuous Bogner-Fox-Schmit (BFS) elements are employed to study the buckling behavior of rectangular plates with multiple cutouts. BFS elements are constructed by taking the tensor product of cubic Hermitian polynomials, and thus, arguably constitute one of the simplest approaches to deriving plate/shell elements. The simplicity, however, comes at the cost of requiring regular/structured discretizations, which significantly restricts their use for applications featuring complex geometrical details. To circumvent this shortcoming, a combination of a fictitious domain approach, in particular the finite cell method (FCM), with BFS elements is proposed. Consequently, a typically geometry-conforming discretization is replaced by a structured Cartesian background mesh in conjunction with a more involved numerical integration of the system matrices. This opens the path to analyzing geometrically more complex structures such as plates with one ore more cutouts. Here, the main focus is on the stability (buckling) analysis of such plates. By means of two numerical examples featuring only one circular cutout, it is shown that the critical load can be obtained with high accuracy using the proposed approach. In this context, the attained numerical results are compared with high-fidelity solutions computed using isogeometric analysis (IGA). Moreover, the position of a circular cutout is optimized to maximize the critical buckling load, before the last example demonstrates the applicability of Cut BFS elements to more complex cutout geometries.


## 1. Introduction

Thin plates and shells of various shapes are widely used in practice, and the availability of different approaches for modeling their mechanical behavior is essential for engineering and research purposes. One of the simplest possibilities to approximate the deformed shape of a plate was suggested by Bogner, Fox and Schmit in Ref. [1]. Based on the use of a bi-cubic Hermitian approximation, $C^1$-continuity is ensured between neighboring elements. It is noteworthy that the approach is also capable of dealing with geometrically nonlinear shell problems [2]. A brief discussion of the theoretical basis of the Bogner-Fox-Schmit (BFS) finite element approximation for plates is provided below in Section 2. Being reliable and efficient in terms of convergence, this approximation strategy, however, imposes certain restrictions on the topology of the finite element mesh, making its use possible only if the geometry of the plate or shell under consideration fulfills some shape regularity requirements. In the present paper, we suggest extending the range of applicability of this finite element scheme by exploiting a fictitious domain approach, in particular the finite cell method (FCM) [3,4]. Therefore, details concerning the basics of fictitious domain methods are provided in Section 4. Releasing the limitations regarding the geometry of the physical domain, the combined approach preserves the main benefits of the BFS finite element scheme, i.e., simplicity of implementation and rapid mesh convergence. Preliminary investigations on that particular topic have been conducted at TU Wien by R. Duy in his Master's thesis [5]. These studies are extended in the paper at hand. Please note that a similar idea has been recently published by Burman et al. [6] in the context of CutFEM. There, the authors demonstrated the accuracy of cut BFS elements for problems in linear elasticity and specifically stressed a greatly increased applicability to problems of practical interest, which might help to re-vitalize this element type.

The proposed computational scheme[1] has the potential to be applied to various kinds of analyses, such as linear and nonlinear static analyses, dynamics analysis and stability analysis, in particular the solution of buckling problems. The latter option makes it a per-

* Corresponding author.
*E-mail address:* yury.vetyukov@tuwien.ac.at (Y. Vetyukov).

[1] Please note that the developed MATLAB code can be obtained from the authors upon request.

https://doi.org/10.1016/j.compstruc.2022.106854
0045-7949/

fect candidate for studying the effect of buckling strength increase observed in plates under compressive or shear loading by introducing cutouts, as first demonstrated by Gracia and Rammerstorfer in [7]. To determine critical values of the load factor, i.e., the buckling load, a generalized eigenvalue problem including the bending stiffness matrix of the plate and the geometric stiffness matrix resulting from an in-plane pre-stressed state [8,9] is solved; for a brief discussion of this topic see Section 3. Focusing on the task of finding the optimal location of the cutout, which maximizes the critical load, we substantially benefit from the key feature of the proposed combined approach: *The finite element mesh remains unchanged, while the position of the cutout is changing.* Although, for each new position of the cutout the intersected finite cells (cut cells) must be determined anew and, consequently, the integration mesh must be updated, no direct user intervention is required, making the proposed approach highly automatic. Hence, a computationally expensive re-meshing of the domain as required by conventional finite element models becomes obsolete.

The outcome of the buckling analysis is validated against other solutions featuring commercial finite element software and an isogeometric model in Section 6. A simple convergence study provides valuable insights regarding the relative accuracy and reliability of the three considered approaches. We also demonstrate the results of a simple parameter optimization regarding the location of the cutout. The computed optimal positions are in qualitative correspondence to the theoretical predictions provided in Ref. [7]. During the analysis, numerical difficulties are met for particular discretizations or locations of the cutout, which are attributed to the appearance of weakly coupled degrees of freedom (degrees of freedom with small support), when just a small fraction of a finite element remains in the physical domain [10]. This issue is particularly pronounced for the considered optimization problem because of the need to change the geometry of the physical domain in small steps. In the present contribution, an engineering-type approach is chosen to circumvent such problems. The stabilization of the proposed method is achieved by choosing a suitable value for the indicator function based on the material properties of the structure. This technique works very well for computing the fundamental buckling mode, but a different technique is required to compute higher buckling modes. Here, a filter based on the physical area of the cut element is suggested (see Appendix A). Elements featuring small cuts are, thus, discarded from the analysis which entails a small error, but greatly enhances the numerical robustness of the simulation. More advanced measures, which are out of the scope of this article would be tailored pre-conditioning procedures using additive Schwarz methods [11] or additional stabilization terms such as the Ghost penalty often used in CutFEM [12]. For the sake of completeness, a convergence analysis for the static plate bending problem is conducted, highlighting the expected optimal convergence of the cut BFS elements (see Appendix C).

## 2. Bogner-Fox-Schmit elements

In the context of structural mechanics, we treat the plate as a material surface with particles representing the cross-sectional fibers of the three-dimensional structure. Allowing for no shear deformation, the classical models of Kirchhoff plates and Kirchhoff–Love shells are based on a kinematic relation between the rotation of particles and the deformation of the surface. Although it is widely accepted that the classical plate model is sufficient for the majority of engineering applications, modeling strategies with independent fields of displacements and rotations possess certain advantages. Thus, the Reissner–Mindlin-Uflyand model [13,14] (also known as first order shear deformation theory; FSDT) allows approximating the rotation of particles and their translatory motion independently. Thus, the kinematic boundary conditions include just the values of the field variables and not their derivatives and, most importantly, the continuity requirements for the finite element approximation are less restrictive than that of the classical model. These advantages, however, are often outweighed by an unnecessary high number of degrees of freedom in the model along with the need to treat the issue of shear locking [15,16] and to deal with complicated constitutive laws featuring essentially more strain measures and stiffness coefficients in comparison to the classical model.

A finite element approximation for a classical Kirchhoff plate model must, strictly speaking, kinematically eliminate the transverse shear, which imposes a smoothness condition at the interfaces between the elements, i.e., the normal to the deformed surface of the plate must not exhibit jumps, and the approximation for the deformed surface must remain $C^1$-continuous. This requirement is, however, partially released in various plate finite elements based on the discrete Kirchhoff theory, see the comprehensive review provided in Ref. [17]. With deflection and rotation variables approximated separately, such elements theoretically converge to the exact solutions of the classical theory. This is due to the fulfillment the "unshearability" on a part of the geometry (e.g., all around the boundary) by means of an appropriate choice of the approximating functions. An extension to curved shells is implemented in commercially available finite element software packages like ANSYS or Abaqus in form of triangular elements, see Ref. [18].

Other options are the use of a discontinuous Galerkin method [19] with jumps of the unit normal vector of the surface across the element boundaries, which are in turn compensated by boundary integral terms, or by applying the technique of Lagrange multipliers [20]. This, however, results in an over-constrained formulation with potential issues regarding the solvability. In the context of rotation-free formulations, it is also possible to impose the smoothness conditions just at the nodes of the finite element mesh [21,22] – the consequence being that only sub-optimal rates of convergence are attained [9]. Finally, we mention several known possibilities for constructing a conforming approximation, which exactly fulfills the $C^1$-continuity condition. The TUBA-family of finite elements [23,24], which has been known already since the year 1968, is a universal solution, whose main drawback is its computational inefficiency because of the high number of degrees of freedom. The idea to construct diverse families of plate and shell elements based on the isogeometric analysis (IGA) paradigm, briefly discussed in Section 5, is nowadays very popular. This is only natural, since the main strength of IGA is providing a straightforward path to develop elements with higher order continuity of the ansatz space [25]. Also subdivision surfaces have been used to develop fully $C^1$-continuous Kirchhoff–Love shell elements [26]. In the present paper, however, we focus on arguably one of the simplest variants of finite element approximations providing the necessary $C^1$-continuity of the deformed surface of the plate, which was suggested in the year 1965 by Bogner, Fox, and Schmit [1]. Specific details of the respective finite element model are discussed in the remainder of this section, see also Refs. [9,2] for further details.

The fundamental equations (and also kinematic boundary conditions) of the classical Kirchhoff plate theory have been known for a long time [27]. They were justified by physical and numerical experiments, and additionally by asymptotic analysis [28]. The single strain measure of a Kirchhoff plate consists in the tensor of curvatures $\boldsymbol{\kappa}$, which equals the second gradient $\nabla$ of the transverse deflection $w$:

$$\boldsymbol{\kappa} = \nabla\nabla w. \tag{1}$$

Introducing the Cartesian coordinates $x, y$ in the plane of the plate with unit basis vectors $\boldsymbol{e}_x$ and $\boldsymbol{e}_y$, we rewrite (1):

$$\boldsymbol{\kappa} = \partial_x^2 w \boldsymbol{e}_x\boldsymbol{e}_x + \partial_x\partial_y w\left(\boldsymbol{e}_x\boldsymbol{e}_y + \boldsymbol{e}_y\boldsymbol{e}_x\right) + \partial_y^2 w \boldsymbol{e}_y\boldsymbol{e}_y, \quad \partial_x \equiv \frac{\partial}{\partial x}, \quad \partial_y \equiv \frac{\partial}{\partial y}. \tag{2}$$

The strain energy of an elastic plate at bending is a functional over the field of deflections:

$$U^{\mathrm{b}}[w(x,y)] = \int_\Omega U \,\mathrm{d}\Omega. \tag{3}$$

Here, $\Omega$ is the physical domain of the plate and $U$ is the strain energy per unit area, which is a quadratic form of the strain measure:

$$U = \frac{1}{2}\left(D\nu(\mathrm{tr}\boldsymbol{\kappa})^2 + D(1-\nu)\mathrm{tr}(\boldsymbol{\kappa}\cdot\boldsymbol{\kappa})\right). \tag{4}$$

The flexural stiffness coefficient $D$ depends on Young's modulus $E$, Poisson's ratio $\nu$ and the thickness $t$ of the homogeneous plate:

$$D = \frac{Et^3}{12(1-\nu^2)}. \tag{5}$$

For a non-smooth, i.e., $C^0$-continuous, displacement field $w(x,y)$, whose first order derivatives experience jumps at the boundaries of the finite elements, the second order derivatives as components of the curvature tensor in (2) would include Dirac's delta functions. This would result in concentrated contributions in the energy integral (3), which are difficult to account for in a numerical procedure.

Aiming to achieve the necessary inter-element continuity of the derivatives of $w(x,y)$, we consider a finite element with four nodes and four degrees of freedom per node, namely

$$w_i, \quad (\partial_\xi w)_i, \quad (\partial_\eta w)_i, \quad (\partial_\xi\partial_\eta w)_i. \tag{6}$$

Here, $i = 1,2,3,4$ is the local number of the node, and $\partial_\xi, \partial_\eta$ are the derivatives with respect to the local coordinates $\xi$ and $\eta$ of the finite element, which are bounded by $-1 \leqslant \xi, \eta \leqslant 1$. Not only the slopes $\partial_\xi w$ and $\partial_\eta w$, but also the mixed second-order derivative $\partial_\xi\partial_\eta w$ is necessary to achieve the desired smoothness. The mapping between the local and global Cartesian coordinate systems needs to be $C^1$-continuous across the element boundaries as well, which imposes certain limitations regarding the topology of the mesh. Exactly four elements must meet in each node, such that a smooth continuation of the coordinate lines $\xi = \text{const}$ or $\eta = \text{const}$ from one element to another can be reached. This is, however, not a problem in the present context of the combined approach, as only regular finite element meshes are considered by definition. In particular, all finite elements are squares with the side length $h$, and thus, the mapping simplifies to

$$x = x_0 + h\xi/2, \quad y = y_0 + h\eta/2, \quad \partial_x = h/2\,\partial_\xi, \quad \partial_y = h/2\,\partial_\eta, \quad \mathrm{d}\Omega = \mathrm{d}x\,\mathrm{d}y = h^2/4\,\mathrm{d}\xi\,\mathrm{d}\eta. \tag{7}$$

Ordering the nodes in counter-clockwise fashion and placing the first node $i = 1$ at $\xi = \eta = -1$ as depicted in Fig. 1, we write an approximation within a finite element in the form

$$w = \sum_{i=1}^{4}\left(w_i S_{i,1}(\xi_1,\xi_2) + (\partial_\xi w)_i S_{i,2}(\xi,\eta) + (\partial_\eta w)_i S_{i,3}(\xi,\eta) + (\partial_\xi\partial_\eta w)_i S_{i,4}(\xi,\eta)\right). \tag{8}$$

The 16 bi-cubic shape functions $S_{i,j}$ and their first-order derivatives (slopes) vanish along those edges of the finite element, which do not include node $i$. At the node itself, they fulfill the natural conditions $S_{i,1} = 1, \partial_\xi S_{i,2} = 1, \partial_\eta S_{i,3} = 1, \partial_\xi\partial_\eta S_{i,4} = 1$ with all other values vanishing, which guarantees that the nodal degrees of freedom indeed retain their physical meaning. Note that the fact that the values of the nodal degrees of freedom do not contribute to the deflections and slopes at the two edges opposing the node at hand is essential for obtaining the desired degree of the inter-element continuity.

As visually demonstrated in Fig. 2, the actual shape functions $S_{1,j}$ for the degrees of freedom of the first node of a finite element are easily constructed as products of the one-dimensional cubic Hermitian polynomials

$$\psi_1(\xi) = \frac{1}{4}(1-\xi)^2(2+\xi), \quad \psi_2(\xi) = \frac{1}{4}(1-\xi)^2(1+\xi). \tag{9}$$

These functions possess the following properties:

$$[\psi_1(-1), \psi_1\prime(-1), \psi_1(1), \psi_1\prime(1)] = [1,0,0,0], \quad [\psi_2(-1), \psi_2\prime(-1), \psi_2(1), \psi_2\prime(1)] = [0,1,0,0]. \tag{10}$$

For a one-dimensional Euler–Bernoulli beam, $\psi_1(\xi)$ corresponds to the shape function connected to the displacement degree of freedom at the first node located at $\xi = -1$, while $\psi_2(\xi)$ accounts for the rotational degree of freedom at the same node. The shape functions related to other nodes are derived by taking the tensor product of all four cubic Hermitian polynomials

$$\begin{aligned} &\psi_1(\xi) = \tfrac{1}{4}(1-\xi)^2(2+\xi), \quad \psi_2(\xi) = \tfrac{1}{4}(1-\xi)^2(1+\xi), \\ &\psi_3(\xi) = \tfrac{1}{4}(1+\xi)^2(2+\xi), \quad \psi_4(\xi) = \tfrac{1}{4}(1+\xi)^2(\xi-1), \end{aligned} \tag{11}$$

in both local coordinates, i.e., $\psi_i(\xi)\psi_j(\eta)$ with $i,j = 1,2,3,4$. Embedding the local numbering of nodes into the global vector of degrees of freedom $q$ of the entire model and computing the integral given in (3) in an element-wise fashion

$$U^{\mathrm{b}}_{\mathrm{e}} = \int_{\Omega_{\mathrm{e}}} U \,\mathrm{d}\Omega \tag{12}$$

using a Gaussian quadrature rule with $3 \times 3$ integration points, we obtain the quadratic form of the total strain energy at bending

$$U^{\mathrm{b}} = \sum_{\text{elements}} U^{\mathrm{b}}_{\mathrm{e}} = \frac{1}{2} q^T K q \tag{13}$$

with the stiffness matrix $K$, which determines the elastic properties of the plate at bending.

## 3. Stability analysis

In linear elasticity, bending and in-plane (membrane) deformations of a homogeneous plate are fully decoupled. It is, however, not necessary to use the entire geometrically nonlinear formulation of the shell theory [29] to obtain the critical membrane stress state, at which the planar configuration becomes unstable. At conservative loading, buckling is associated with the bifurcation of the equilibrium path, such that small bending becomes possible in the absence of transverse loading, i.e., the solution becomes non-unique, and the transverse stiffness of the structure vanishes.

Small bending of a plate under the simultaneous action of a transverse distributed force $f(x,y)$ and the tensor of membrane stress resultants $\boldsymbol{N}$ is governed by the following equation for the transverse deflection $w$:

$$D\Delta\Delta w - \nabla\cdot(\boldsymbol{N}\cdot\nabla w) = f. \tag{14}$$

Being referred to as the von Kármán plate theory [30], this equation follows from the incremental theory of shells, in which the generally nonlinear equations are linearized, and thus, allows us to consider a small deformation superimposed upon a finite one [9, p. 143]. Interestingly, Timoshenko and Woinowsky-Krieger [27, p. 380] mention,

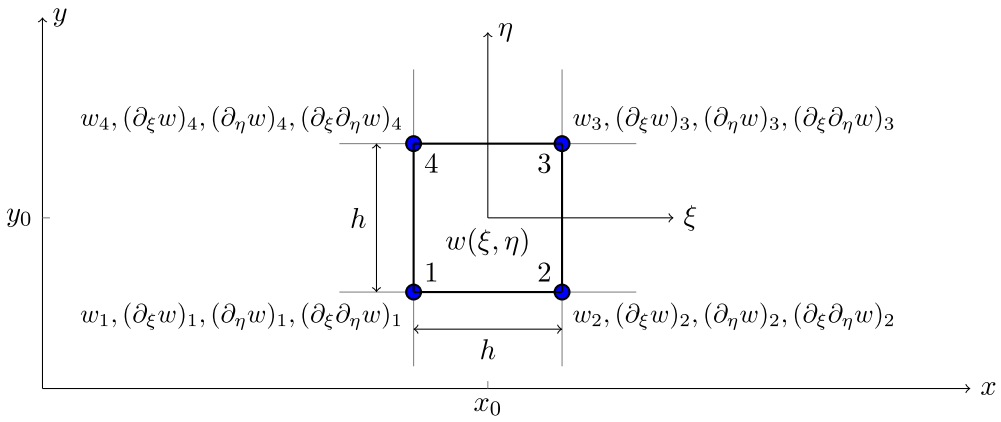


**Fig. 1.** Square BFS finite element with local numbering of nodes and nodal degrees of freedom, embedded both in the global coordinate system $x,\ y$ and the local one $\xi, \eta$.

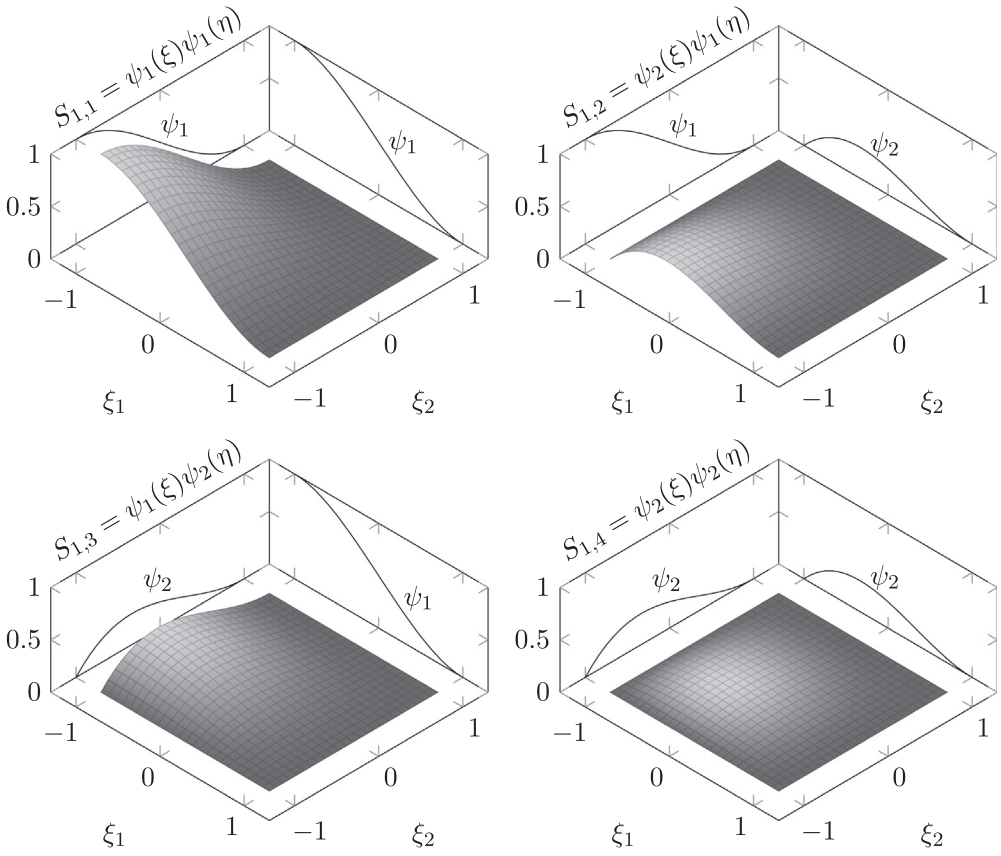


**Fig. 2.** Bi-cubic shape functions of the first node of a BFS finite element.

that this equation in the coordinate form has been derived by Saint–Venant in his translation of the original work by Alfred Clebsch [31]. For thin plates, the respective in-plane deformation in the critical state is small and can be ignored, so that the differential operators $\nabla$ and $\Delta \equiv \nabla \cdot \nabla$ are considered with respect to the coordinates of the undeformed state $x, y$ as in the linear theory of elasticity. Note, that the in-plane stress resultants $\boldsymbol{N}$ are considered for a through-the-thickness element of a plate, i.e., they are the integrals of the three-dimensional stresses over the thickness and hence, feature the unit force per length [N/m]. The in-plane loading is critical and leads to buckling, if the corresponding stress field $\boldsymbol{N}$, which follows as a solution of the plane problem of elasticity, allows for a non-trivial solution $w \neq 0$ of the homogeneous version of (14), i.e., in the absence of transverse forces ($f = 0$). The problem must certainly be considered for particular boundary conditions, both for the in-plane stress and for the transverse bending.

Energy considerations play an important role in the theory of elastic stability. The energy of a plate with membrane stresses, which is associated with a given deflection field $w(x, y)$, is known to be [32,33]

$$U^{\text{total}}[w] = U^{\text{b}}[w] + U^{\text{m}}[w] + U^{\text{ext}}[w]. \tag{15}$$

While the first term, which arises because of the bending stiffness of the plate, shall be computed according to (3) (or (13) in the discretized model), the contribution caused by the in-plane loading takes the following form

$$U^{\mathrm{m}} = \frac{1}{2}\int_{\Omega} \nabla w \cdot \boldsymbol{N} \cdot \nabla w \,\mathrm{d}\Omega = \frac{1}{2}\int_{\Omega} \left( N_x (\partial_x w)^2 + N_y (\partial_y w)^2 + 2N_{xy}\,\partial_x w\,\partial_y w \right) \mathrm{d}\Omega. \tag{16}$$

The potential energy of the external forces has a simple expression

$$U^{\mathrm{ext}} = -\int_{\Omega} f w \,\mathrm{d}\Omega. \tag{17}$$

Indeed, the differential equation provided by (14) is a Euler-Lagrange equation for the variational formulation

$$\delta U^{\mathrm{total}} = 0, \tag{18}$$

which means that the total strain energy is at minimum in the state of static equilibrium. The basic idea behind the linear buckling analysis is, that the external loading in the plane of the plate is considered being proportional to a single load factor $\lambda$ [34]. Because of the linearity, the membrane stress resultants are also proportional to this factor:

$$\boldsymbol{N} = \lambda \tilde{\boldsymbol{N}}. \tag{19}$$

Consequently, the distribution of the membrane stress resultants $\tilde{\boldsymbol{N}}$, which corresponds to the unit value of the load factor, shall be determined once in at beginning of the procedure. Substituting (19) into the partial differential Eq. (14) with $f = 0$ and taking specific boundary conditions for $w$ into account, we obtain an eigenvalue problem for $\lambda$. Thus, we can determine the minimal value of the force factor, at which the homogeneous boundary value problem allows for a non-trivial solution $w \neq 0$. This is the critical load factor $\lambda_*$. Note that the planar configuration remains stable as long as $\lambda < \lambda_*$, and becomes unstable afterwards.

In the numerical approach, we deal with the weak form of the problem, which features the energy expressions given in (15). The contribution due to the membrane stress resultants are also scaled with the load factor:

$$U^{\mathrm{m}} = \lambda \tilde{U}^{\mathrm{m}}, \quad \tilde{U}^{\mathrm{m}} = \frac{1}{2}\int_{\Omega} \nabla w \cdot \tilde{\boldsymbol{N}} \cdot \nabla w \,\mathrm{d}\Omega. \tag{20}$$

In the discretized form, the integral results in a quadratic form for the degrees of freedom of the finite element model

$$\tilde{U}^{\mathrm{m}} = \frac{1}{2} q^T K_N q \tag{21}$$

with $K_N$ being the geometric stiffness matrix [34], which is computed once for the unit value of the load factor. In the absence of external loading, the total energy of the plate – see (15) – becomes

$$U^{\mathrm{total}} = \frac{1}{2} q^T (K + \lambda K_N) q. \tag{22}$$

The stationarity condition for the static equilibrium, given by (18), results in a homogeneous algebraic system of equations

$$(K + \lambda K_N) q = 0, \tag{23}$$

which is only solvable if $\lambda$ belongs to the spectrum of the generalized eigenvalue problem with the conventional bending stiffness matrix $K$ and the geometric stiffness matrix $K_N$. We are of course interested in the minimal value $\lambda_*$, at which the discretized model allows for a non-trivial solution, i.e., $q \neq 0$ when $\det(K + \lambda K_N) = 0$. Note that the matrix $K + \lambda K_N$ is closely related to the tangent stiffness matrix of the fully geometrically nonlinear formulation, see Ref. [8].

It needs to be mentioned, that it is very convenient to use the same discretization for both the bending problem and the plane stress problem. The latter problem is solved at the preliminary stage of the analysis (see the simulation workflow provided in Section 6.1). To this end, we discretize the two components of the in-plane displacement field

$$\mathbf{u} = u\,\mathbf{e}_x + v\,\mathbf{e}_y \tag{24}$$

using the same bi-cubic shape functions as given in (8) and thus, introducing eight nodal degrees of freedom

$$u_i, \quad v_i, \quad (\partial_\xi u)_i, \quad (\partial_\xi v)_i, \quad (\partial_\eta u)_i, \quad (\partial_\eta v)_i, \quad (\partial_\xi \partial_\eta u)_i, \quad (\partial_\xi \partial_\eta v)_i. \tag{25}$$

The linear in-plane problem is then solved for the unit value of the load factor $\lambda = 1$, which provides the stress resultants $\tilde{\boldsymbol{N}}$ directly at the integration points of the mesh (which are in general determined by the configuration of the finite cells). This is very convenient, since these values are simply stored and later re-used for computing the integral in (20) and the geometric stiffness matrix $K_N$. Obviously, the fictitious domain concept, as discussed in Section 4, is also applied for solving the in-plane problem. Although inter-element $C^1$-continuity is not required for solving the plane stress problem of elasticity, the approach is advantageous for three reasons: There are the possibilities to (i) re-use parts of the simulation code, (ii) evaluate $\tilde{\boldsymbol{N}}$ with highest possible accuracy right at the integration points of the plate model and, (iii) obtain a high rate of mesh convergence resulting from the use of bi-cubic shape functions.

## 4. Fictitious domain concept

As discussed in Section 2, BFS elements suffer from the fact that they require a regular topology of the mesh to ensure $C^1$-continuity between neighboring elements. This is a severe limitation regarding the geometry of the physical domain, which restricts the use of this type of plate elements for problems of practical interest. On the other hand, we should also keep in mind that the formulation of BFS elements is very simple and the convergence properties are generally acknowledged to be excellent, surpassing most other formulations. Consequently, we can state with good reason that BFS elements constitute a very efficient approach to handle thin plate/shell problems [8, p. 151ff.]. Provided that the geometry meets the requirements mentioned before, we note that the theoretically expected convergence rates are attained in numerical examples. In order to extend the range of applicability of BFS elements and thus, to re-vitalize them, we propose a combination of BFS elements with a fictitious domain approach. This overcomes the regular mesh issue as fictitious domain methods commonly exploit Cartesian meshes to spatially discretize a structure. Thus, we can leverage the exceptional accuracy and simplicity of BFS elements, while being able to take into account arbitrarily complex geometries in an automatic manner without any user intervention.

The fundamental idea of fictitious domain methods, and the finite cell method (FCM) in particular, is to solve the governing equations on an extended domain $\Omega^{\mathrm{ex}}$, which replaces the original physical domain $\Omega_{\mathrm{phys}}$ for the numerical analysis. While $\Omega_{\mathrm{phys}}$ can exhibit an arbitrarily complex shape, $\Omega^{\mathrm{ex}}$ is typically of regular shape (cf. Fig. 3). Note that the following explanations are strictly limited to void regions within the extended domain. For multi-material problems more advanced solution strategies are required and a local enrichment of the ansatz space is inevitable [35]. If only voids are considered, the extended domain $\Omega^{\mathrm{ex}}$ is the union of the physical domain $\Omega_{\mathrm{phys}}$ and the so-called fictitious domain $\Omega_{\mathrm{fict}}$. From a numerical point of view, it is clear that the additional fictitious domain should not add any stiffness to the system in order to obtain the same solution as for the initial problem. To this end, an indicator function $\alpha(\mathbf{x})$ is introduced, which takes the value of 1 in the physical domain, while it is equal to 0 in the fictitious domain

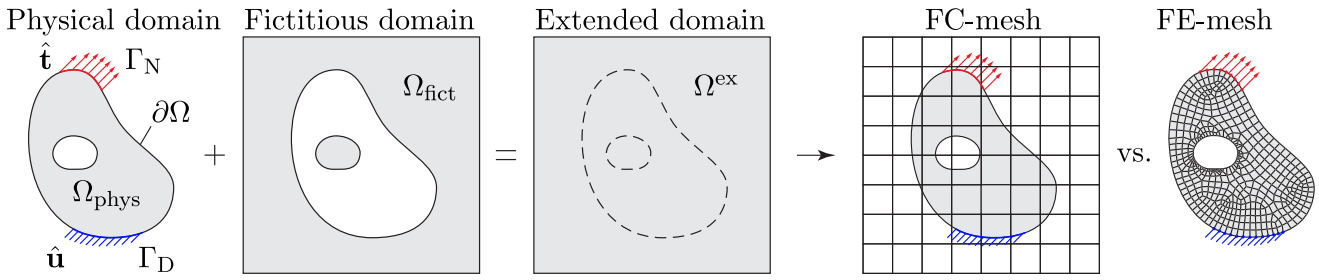


**Fig. 3.** Fundamental idea of fictitious domain methods (Cartesian mesh) in comparison to a typical finite element discretization (body-fitted mesh).

$$\alpha(\mathbf{x}) = \begin{cases} 1.0, & \forall\, \mathbf{x} \in \Omega_{phys} \\ 0.0, & \forall\, \mathbf{x} \in \Omega_{fict} \end{cases} \tag{26}$$

All volume integrals that arise in the weak form of the governing equations (e.g., to compute the stiffness matrix, body forces, etc.) are now multiplied with $\alpha(\mathbf{x})$

$$\int_{\Omega_{phys}} \mathscr{P}(\mathbf{x}) \mathrm{d}\Omega = \int_{\Omega^{ex}} \alpha(\mathbf{x}) \mathscr{P}(\mathbf{x}) \mathrm{d}\Omega. \tag{27}$$

The immediate effect of the indicator function on the solution of (27) is that, while we have a regular integration domain, a discontinuous integrand is introduced for all elements that are cut by the physical boundary. These elements, to better distinguish them from conventional finite elements, are called cut cells (see Fig. 4) and require a special treatment. It is well-known that the standard Gaussian quadrature rules that are used in FEM do not cope well with discontinuous integrands and therefore, a special integration strategy must be devised. In the context of FCM, a spacetree based decomposition of the integration domain is often favored due to its robustness. Other approaches include the derivation of special integration rules for cut cells by means of moment fitting [36], the application of the divergence theorem to reduce the dimensionality of the problem [37], the generation of a geometry-aligned integration mesh [38,39], etc. Thus, it can be stated that the meshing problem is avoided by taking more sophisticated integration schemes into account. For a comprehensive review on different integration approaches, the reader is referred to Refs. [40,41]. For an in-depth discussion of the FCM and its applications the review articles by Schillinger and co-workers [42,43] are recommended, while a mathematical analysis of the convergence properties is provided in Ref. [44]. For a more comprehensive presentation of BFS elements in combination with FCM in terms of its numerical implementation, the reader is referred to Ref. [5].

At this point, we only sketch the basic idea of the standard quadtree-based sub-cell integration technique as discussed in Ref. [41], which is implemented for the cut BFS elements. Since Gaussian quadrature rules are not efficient when handling discontinuous integrands, the domain must be subdivided recursively to reduce the integration error. This approach is illustrated in Fig. 5 for the cut cell highlighted in Fig. 4. The quadtree decomposition is executed for different refinement levels $k$. We clearly observe that the smallest cells (leaf cells) are accumulated around the boundary of the physical domain such that a composed Gaussian integration rule yields accurate results. Each of the sub-cells (which are strictly used for integration purposes) features its own coordinate system $(r, s)$ and is fitted with $(p+1)^2$ integration points, where $p$ is the polynomial degree of the shape functions ($p = 3$). Thus, (27) is re-written on an element-level as

$$\int_{\Omega_e} \alpha(\mathbf{x}) \mathscr{P}(\mathbf{x}) \mathrm{d}\Omega = \sum_{i=1}^{n_{sc}} \sum_{j=1}^{n_{IP}} \alpha(\mathbf{x}(\xi_{ij}(\mathbf{r}_j))) \mathscr{P}(\mathbf{x}(\xi_{ij}(\mathbf{r}_j))) w_{ij}, \tag{28}$$

where $\mathbf{r}$ is the vector of the sub-cell coordinate system, $\xi$ denotes the vector of the element coordinate system, and $\mathbf{x}$ stands for the vector of global coordinates (see Fig. 6). The integration weight $w_{ij}$ has to be distinguished from the weight of the standard Gaussian quadrature rules, as it is composed of integration weight multiplied with the determinants of the Jacobian matrices for the two mappings from the sub-cell to the element and finally to the global space. More details on the implementation and accuracy of the integration technique are given in Ref. [41], while a mathematically concise convergence proof is provided in Ref. [44], demonstrating that the theoretically optimal rate is attained if the numerical integration is accurate enough.

In a nutshell, the idea of decoupling the geometry approximation from the spatial discretization provides a path to extend the possible range of applications for BFS elements. By exploiting the

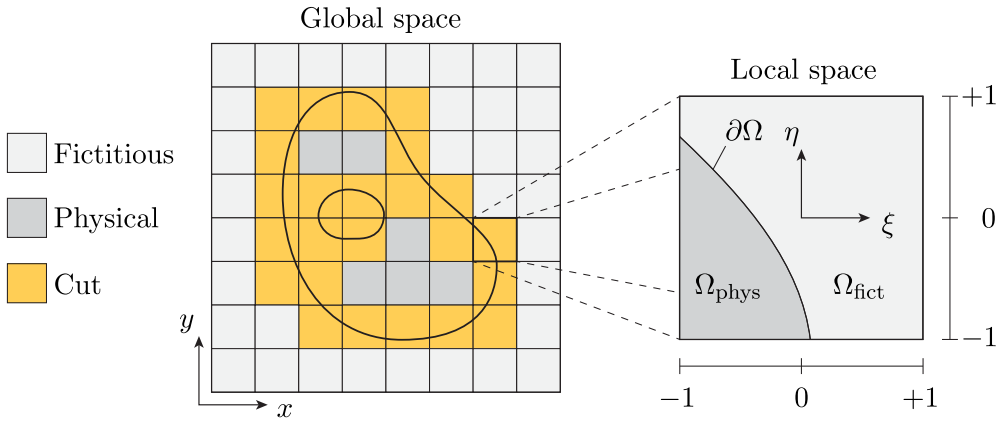


**Fig. 4.** Physical, fictitious, and cut cells in the global and local coordinate systems.

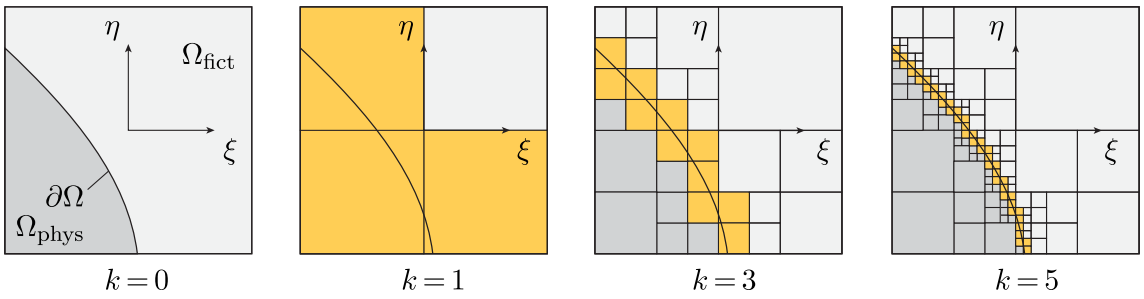


**Fig. 5.** Construction of the element-level integration grid based on the quadtree decomposition of a cut element. Three different refinement levels $k = 1, 3, 5$ are depicted.

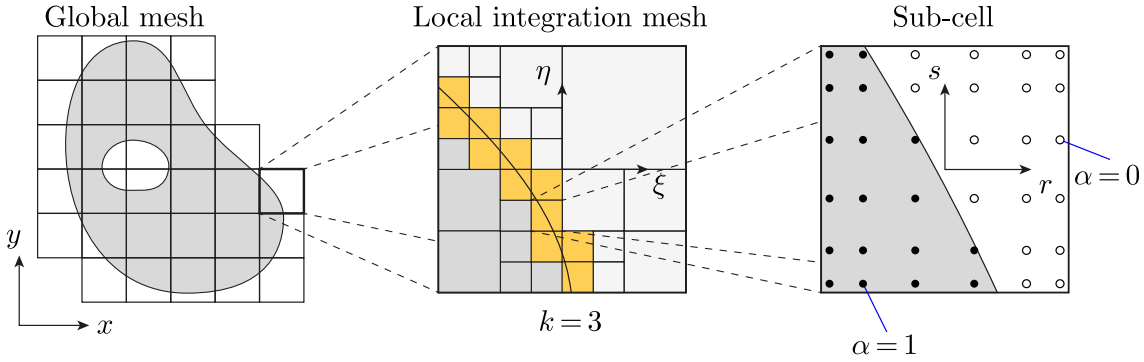


**Fig. 6.** Illustration of the different coordinate spaces used in the quadtree-based numerical integration.

fictitious domain concept, the need for a regular mesh does not pose any limitation, but is a requirement to circumvent the meshing problem. We will make good use of this new freedom and apply it to the buckling analysis of thin plates. Here, the excellent numerical properties of BFS elements in combination with the flexibility of fictitious domain methods provides a neat way to analyse different plate configurations.

## 5. Isogeometric analysis

Isogeometric analysis (IGA) is a relatively new paradigm in computational mechanics, featuring higher order continuity properties by adopting non-uniform rational B-splines (NURBS) as basis functions [45]. Thus, IGA enables efficient discretizations of Kirchhoff plates and Kirchhoff–Love shells [46], and is used in this paper for computing reference solutions in Section 6. We deploy an isogeometric Kirchhoff–Love shell element [25,47], which contains the Kirchhoff plate formulation as a special case, and is also capable of calculating the geometric stiffness matrix required for buckling analysis.

Despite the high flexibility of NURBS in geometric modeling, the geometries considered in Section 6 pose a challenge when it comes to describing them by means of a fully $C^1$-continuous parametrization. In CAD modeling, such geometries would typically be obtained via trimming, which, for analysis purposes, requires special integration rules for trimmed elements, similar to the case of cut elements discussed in Section 4. Several approaches have been proposed for the integration of trimmed elements (see, e.g., Refs. [48–51]), among them also the FCM, discussed briefly in Section 4. Alternatively, such geometries can be modeled relatively easily by using multiple patches or single patches containing lines of $C^0$-continuity in the parametrization. In these cases, the required $C^1$-continuity needs to be enforced through additional terms, e.g., by penalty [52,53], Nitsche [54,51], or mortar [55,56] methods, which, however, might introduce an additional error in the solution. For the scope of this paper, we developed a fully $C^1$-continuous single patch modeling approach for square plates with circular cutouts. The approach is parametrized such that arbitrary variations of the geometry (plate dimensions, cutout radius, and location) can be taken into account. The detailed procedure is presented in Appendix B.

## 6. Numerical examples

The numerical behavior of the proposed cut BFS element in application to buckling analysis is investigated in detail in this section. Note that for the sake of completeness, a convergence analysis for a static plate bending problem has been conducted as well and is discussed in Appendix C. The numerical results highlight that optimal rates of convergence are achievable by employing the proposed cut BFS elements. However, before we delve into the topic of buckling analysis a few comments regarding the numerical implementation to guarantee a robust solution of the eigenvalue problem are in order (see Section 6.1). Thereafter, the numerical properties of cut BFS elements are comprehensively assessed. To this end, a square plate with a circular cutout is studied under two different load cases (see Section 6.2), i.e., uniaxial compression and pure shear. The results obtained by employing cut BFS elements are verified against numerical overkill solutions that have been generated using the commercial software Abaqus and an in-house IGA model with exact geometry description (polynomial degrees: $p = q = 6$, number of degrees of freedom: 220,698; see Appendix B). In the next step, the maximal buckling load for a square plate is computed depending on the location of a circular cutout with fixed radius (see Section 6.3). Here, it is shown that an increase of the critical load can be achieved despite introducing a hole in the structure. Similar findings have also been reported in Refs. [57,7]. This result is obviously also influenced by the size of the void region with respect to the size of the plate under investigation. As a last example, a rectangular plate with multiple cutouts (see Section 6.4) is analyzed to demonstrate the capabilities of the

proposed methodology for analyzing geometrically more complex structures.

### 6.1. Implementational aspects

Before discussing the numerical results, a few comments regarding the implementation and solution of the eigenvalue problem for the buckling load are necessary. The overall simulation workflow consists of the following five steps:

1. The finite element mesh and the spacetree decomposition of the integration domain for solving both the plane stress and the plate buckling problems are initialized.
2. Solving the linear plane stress problem of elasticity, we obtain the in-plane nodal degrees of freedom as in (25). The elastic response to the unit load provides the distribution of the stress resultants $\tilde{\boldsymbol{N}}$. Note that the distortion of the physical domain because of the in-plane displacement field $\mathbf{u}$ is neglected in the linear buckling analysis [34].
3. The geometric stiffness matrix $K_N$ follows as the quadratic form $\widetilde{U}^{\mathrm{m}}$ is assembled according to (20). The argument of the quadratic form $q$ comprises the nodal degrees of freedom of the plate problem as introduced in (6).
4. The elastic stiffness matrix of the plate $K$ is obtained by assembling the strain energy of bending of the plate model $U^{\mathrm{b}}$ according to (12).
5. The critical load factor is sought as the minimal eigenvalue $\lambda_*$ of the generalized eigenvalue problem for the matrices $K$ and $K_N$. At $\lambda = \lambda_*$, the homogeneous equilibrium problem given by (23) allows for a non-trivial solution $q_*$, which determines the first buckling mode.

The examples considered below feature simply-supported edges in the plate buckling problem. These kinematic boundary conditions require constraining two degrees of freedom of the nodes on the edges: either $w_i$ and $(\partial_\xi w)_i$ on the horizontal edges, which are (for regular Cartesian meshes) identical to the coordinate lines of the local coordinate $\xi$, or $w_i$ and $(\partial_\eta w)_i$ on the vertical edges. This guarantees fulfilling the physical boundary condition $w = 0$ along the entire edge and not only in the nodes. In case of a clamped edge, the vanishing slope in the direction normal to the boundary would consistently be achieved by constraining all four degrees of freedom of the respective nodes. In the framework of the fictitious domain approaches, Nitsche's method [58–60] is employed to handle kinematic boundary conditions (in a weak sense) at the inclined or curved edges, not coinciding with the boundaries of the elements; a specific implementation and validation of this approach for BFS elements is a subject of future research.

Finally, we also shortly comment on the specific issue of the fictitious domain method, which becomes particularly pronounced during eigenvalue analyses when solving buckling or eigenfrequency problems. As mentioned before in Section 1, depending on the position of the void in the mesh, cut elements can be generated that contribute only a very small amount to the physical domain. Thus, some degrees of freedom exhibit only a small support, which leads to conditioning problems and also nonphysical results in the analysis. Possible solutions to this problem consist in (i) either using additional stabilization terms [6] or (ii) employing tailored pre-conditioners [11]. However, none of these techniques have been tested and analysed for eigenvalue problems yet and therefore, a simple, engineering-type solution is proposed in this contribution.

First, let us recall the definition of the indicator function $\alpha(\mathbf{x})$ provided by (26), which is given at this point in a slightly changed version:

$$\alpha(\mathbf{x}) = \begin{cases} 1.0, & \forall\, \mathbf{x} \in \Omega_{\text{phys}} \\ \alpha_0, & \forall\, \mathbf{x} \in \Omega_{\text{fict}} \end{cases} \tag{29}$$

Instead of choosing a value of exactly 0 for points located in the fictitious domain, it is customary to use a very small value, i.e., $\alpha_0 = 10^{-\gamma}$, where $\gamma$ commonly assumes values between 4 and 12. Thus, the effect of the fictitious on the physical domain is limited, while still guaranteeing accurate results without compromising the robustness of the method. In our implementation, we select a value based on the material properties, similar to the suggestion put forward in Ref. [58],

$$\begin{aligned} \gamma &= \left\lfloor \log_{10}\left( \frac{E}{2(1+\nu)(1-2\nu)}\ \mathtt{eps} \right) \right\rceil \\ &= \left\lfloor \log_{10}\left( (\lambda_{\mathrm{L}} + \mu_{\mathrm{L}})\ \mathtt{eps} \right) \right\rceil, \end{aligned} \tag{30}$$

where eps denotes machine precision (i.e., $2^{-52} \approx 2.22045 \times 10^{-16}$), while $\lambda_{\mathrm{L}}$ and $\mu_{\mathrm{L}}$ are Lamé's constants. When choosing steel as the plate's material a $\gamma$-value of 4 is obtained. This value is especially critical for eigenvalue analyses to avoid spurious mode shapes in the solution. In a nutshell, it can be stated that the smaller the absolute value of $\gamma$, the smaller is the number of nonphysical results (see Fig. A.1). We need to stress at this point, by applying (30) to select a suitable value for $\alpha_0$, the minimal buckling load is accurately predicted for *all* examples studied in this article. However, if higher order buckling modes are also of interest, i.e., we want to compute the first $n$ buckling modes, spurious results might still be part of the solution spectrum despite the increased value of $\gamma$. Therefore, additional filtering techniques must be applied to obtain accurate and reliable results, see Appendix A for further details.

### 6.2. Buckling analysis of a square plate with a circular cutout

The first numerical example is used to highlight the convergence properties of the proposed element and to verify its accuracy in comparison with solutions obtained from Abaqus and IGA. To this end, a simple square plate including a circular cutout, as suggested in Refs. [7,5], is selected. The plate has an edge length of $l_{\mathrm{x}} = l_{\mathrm{y}} = 1$ m and a thickness of $t = 1$ mm. For the analysis, two load cases (LC) have been defined to compute the critical load, i.e., uniaxial compression (LC1) and pure shear loading (LC2); the external loads (unit force per length; [N/m]) are applied along the edges of the structure as indicated in Fig. 7. A homogeneous and isotropic (linear-elastic) material behaviour is assumed for the remainder of this section and the material properties of steel are employed, i.e., $E = 210$ GPa and $\nu = 0.3$.

In order to account for the circular hole, the indicator function is defined by means of an implicit function similar to the level-set method [61]

$$\alpha(\mathbf{x}) = \begin{cases} 1.0, & \text{if } \mathfrak{L}(\mathbf{x}) \geqslant 0 \\ 0.0, & \text{if } \mathfrak{L}(\mathbf{x}) < 0 \end{cases}, \quad \text{with } \mathfrak{L}(\mathbf{x}) = (x - x_{\mathrm{c}})^2 + (y - y_{\mathrm{c}})^2 - r^2, \tag{31}$$

where $(x_{\mathrm{c}}, y_{\mathrm{c}})$ denotes the position of the center of the circle and $r$ its radius. For the following investigations, two different set ups have been selected:

- Plate 1 (P1): $x_{\mathrm{c}} = 0.5$ m, $y_{\mathrm{c}} = 0.5$ m, $r = 0.15$ m,
- Plate 2 (P2): $x_{\mathrm{c}} = 0.9$ m, $y_{\mathrm{c}} = 0.5$ m, $r = 0.055$ m.

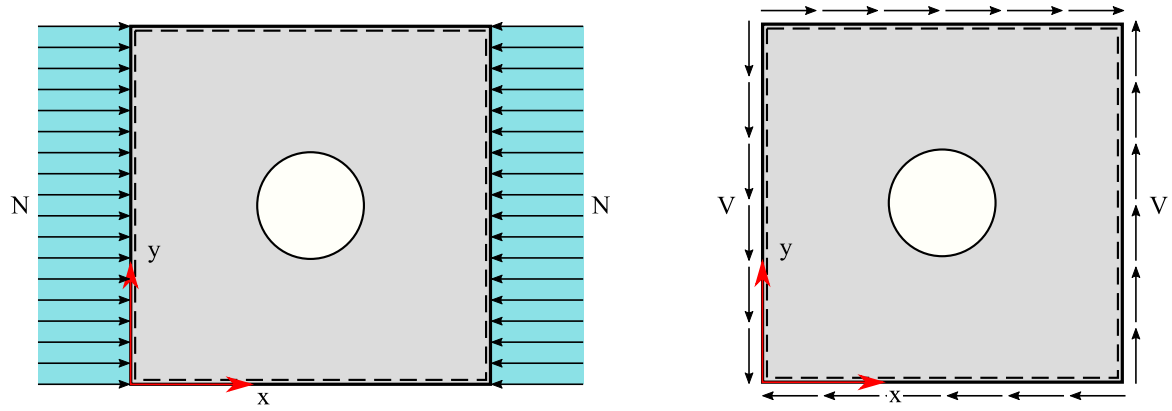


(a) Uniaxial compression (b) Pure shear

**Fig. 7.** Simply-supported square plate (SSSS) with circular cutout subjected to different in-plane load cases.

In terms of kinematic constraints, both in-plane displacement degrees of freedom $u$ and $v$ are fixed at the node at (0,0), while only the displacement in $y$-direction is restricted at the node at ($l_x$,0). This is done to avoid rigid body motions of the plate and thus, guarantee the uniqueness of the solution of the plane stress problem in the absence of kinematic boundary conditions. As a consequence, three degrees of freedom are deleted from the system. Considering the kinematic boundary conditions for the plate problem, we constrain the out-of-plane displacements for all four edges. Additionally, the first derivatives parallel to the plate edges are fixed, i.e., the first derivative with respect to $y$ is constrained for the two vertical edges, while the the first derivative with respect to $x$ is locked for the two horizontal edges. These boundary conditions correspond to a simply-supported boundary condition on all four edges of the plate (SSSS).

In order to assess whether the critical load is in- or decreased due to the introduced cutout [7], we need to determine the buckling load for an intact plate first. In the case of uniaxial compression (LC1), an analytical solution for a simply-supported plate is readily available [62]

$$\sigma_{cr} = \frac{D\pi^2}{t\,l_y^2}\left(\frac{m\,l_y}{l_x}+\frac{n^2 l_x}{m\,l_y}\right)^2, \tag{32}$$

where $m$ and $n$ denote the number of half-waves of buckling in the x- and y-directions respectively. For a square plate ($l_x = l_y$) and the smallest buckling load ($n = m = 1$) (32) simplifies to

$$\sigma_{cr} = 4\frac{D\pi^2}{t\,l_x^2}. \tag{33}$$

Using (33), the critical load, which is given as a pressure load, is computed as 759.2 kN/m$^2$ for our specific configuration. When a pure shear stress state is induced, the critical load cannot be determined analytically and therefore, we have to fall back on empirical formulae, which are based on experimental data. Thus the critical load under pure shear can be determined as [63]

$$\tau_{cr} = K_e E\left(\frac{t}{b}\right)^2, \tag{34}$$

where $K_e$ depends on the support of the plate edges and $b$ is the length of the shorter side. For a Poisson's ratio of $\nu = 0.3$ and simply-supported edges, the value of $K_e$ is determined as approximately 8.43 [64] and thus, (34) yields a critical load, which is given as a surface traction, of 1769.7 kN/m$^2$. Keep in mind, the provided critical pressure and surface traction values $\sigma_{cr}$ and $\tau_{cr}$ need to be multiplied by the thickness of the plate $t$ to obtain the equivalent normal load $N$ or shear load $V$, respectively, which are defined as force per unit edge length and thus have the dimension of [N/m].

#### 6.2.1. Uniaxial compression

The first load case (LC1), constitutes the buckling analysis of a simply-supported plate under uniaxial compression with a circular cutout. The convergence behaviour is assessed with respect to a high-fidelity solution obtained using IGA. The IGA reference value for the load multiplier[2] related to the geometrical set-up P1 is 612.43805, while it is 765.13849 for P2. These results already indicate that there are configurations, where the fundamental buckling load is slightly increased (e.g., P2) despite the circular hole, while in other examples (e.g., P1) significant reductions in the load bearing capacity before buckling are observed.

In Fig. 8, the convergence of the fundamental buckling load with respect to the IGA reference solution is depicted. It can be observed that the results are almost independent of the subcell refinement level for $k \geqslant 2$. In order to assess the convergence behaviour, an $h$-extension is performed, where the square plate under investigation is subdivided into $n_e \times n_e$ elements, with $n_e \in \{4, 8, 16, \ldots, 1024\}$. Thus, an error of well below $10^{-4}\%$ in the critical load can be achieved for both examples. At a later point (even finer spatial discretization), the integration error starts to dominate the overall numerical error in the model and therefore, an error plateau is typically reached as discussed in Ref. [44]. Note that these results have been obtained without applying the filtering techniques discussed in Appendix A. In addition to the convergence study using the proposed cut BFS elements, we also included the results obtained with the commercial FEA software Abaqus. Here, quadrilateral `S8R5` elements, have been employed, which are 8-node thin shell elements featuring 5 degrees of freedom per node, where a reduced integration technique is applied to compute the stiffness matrix. The numerical results obtained by utilizing Abaqus show a peculiar behavior in that a divergence is observed for very fine meshes. That is to say, by increasing the number of degrees of freedom the Abaqus model seems to get softer and thus, the computed buckling load decreases. This is related to the fact that the `S8R5` elements are not *a priori* $C^1$-continuous along their edges, which is enforced by additional penalty terms. Thus, no convergence in a strictly mathematical sense

[2] Remark: The analytical solutions, as detailed in this section, are given in terms of surface loads (pressure loads or surface tractions). However, for the sake of clarity of the presentation, we will provide the load multiplier $\lambda$ for the subsequent analyses — as defined in (23) — instead of the values of the applied surface loads.

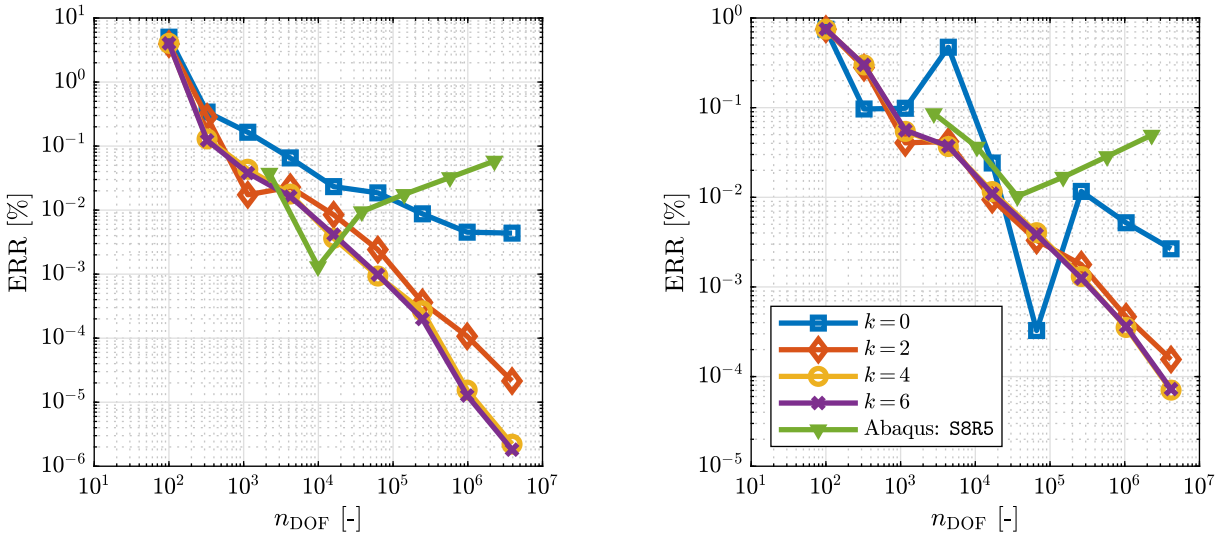


(a) Uniaxial compression (LC1) — P1 (b) Uniaxial compression (LC1) — P2

**Fig. 8.** Error in the critical load for a square plate with a circular cutout under uniaxial compression.

can be achieved. However, the obtained accuracy is sufficient for engineering applications.

*6.2.2. Pure shear*

The second load case (LC2), constitutes the buckling analysis of a simply-supported plate under pure shear loading. As in the previous section, the convergence is evaluated based on an IGA reference solution. The IGA reference values of the load multiplier related to plates P1 and P2 are 1035.4682 and 1783.3341, respectively. Here, a similar behavior compared to the uniaxial compression case is observed. Note that again the buckling load is increased for configuration P2, while it is drastically reduced for the first setup P1.

In Fig. 9, the convergence of the fundamental buckling load with respect to the IGA reference solution is depicted. It can be observed that the results are virtually independent of the subcell refinement level for $k \geqslant 2$. In order to assess the convergence behavior, an $h$-extension is performed, where the square plate under investigation is subdivided into $n_e \times n_e$ elements, with $n_e \in \{4, 8, 16, \ldots, 1024\}$. Thus, an error well below $10^{-3}\%$ in the critical load can be achieved for both examples. In contrast to the uniaxial compression case, a smooth and monotonic convergence is observed. However, the attainable errors are slightly higher. A somewhat surprising finding, which is not fully understood and only occurs for this configuration, is that the most accurate results are obtained without applying a special integration technique, i.e., for $k = 0$. Due to the generally oscillatory convergence of the results for $k = 0$, one possible conjecture is that for some spatial discretizations the numerical solution is getting close to the exact one just by coincidence. However, additional investigations are needed to clarify this issue. Again, these results have been obtained without applying the filtering technique discussed in Appendix A. The conclusions that have been drawn regarding the use of Abaqus' `S8R5` element are confirmed also for the pure shear case, as the solution again diverges for fine spatial discretizations.

*6.3. Maximal buckling load of a square plate with a circular cutout*

In a recent article by Gracia and Rammerstorfer [7], it has been shown how the position of cutouts influences the buckling strength. An increase in the buckling load can be achieved by introducing holes in certain regions of the plate. These findings are related to the concept of "sensor holes"[3] and should also be verified for cutouts of finite dimensions. To this end, a simple brute force optimization approach is utilized to determine the maximum buckling load in a square plate with a circular cutout. The obtained results are then qualitatively compared to the solution provided by Gracia and Rammerstorfer. Since we want to determine the regions, in which cutouts are ideally located, it does not make too much sense to apply advanced optimization techniques. In this case, we would obtain the maximum or minimum critical loads, but could not identify regions of increased or decreased values with respect to the intact plate. However, we are going to exploit existing symmetry properties of the problem to minimize the computational effort. To this end, only the locations marked in red in Fig. 10 are taken into account. Again, we want to stress that to obtain the fundamental buckling load for this example no filtering techniques, as discussed in Appendix A, are required. Keep in mind that these techniques are pre-dominantly needed for reliably calculating higher order modes.

For the subsequent analyses, the radius is set to either $r_1 = 0.055$ m or $r_2 = 0.15$ m (identical to the previous examples) and the center of the circle can be located in the regions $\mathscr{A}_1 = [0.1, 0.9] \times [0.1, 0.9]$ or $\mathscr{A}_2 = [0.2, 0.8] \times [0.2, 0.8]$ to allow for a minimal distance to the edge of the plate. Here, it is assumed that the edge will not be cut such that the outer boundary stays intact. As in the previous section, we will study both load cases, i.e., uniaxial compression and pure shear. Based on the findings discussed in Section 6.2, we choose a sub-cell refinement level $k = 2$ for both load cases. Regarding the spatial discretization, the number of elements per coordinate direction is chosen as $n_e^{\text{comp}} = 16$ for the uniaxial compression case, while it is $n_e^{\text{shear}} = 64$ for the pure shear loading. According to the convergence results presented in Figs. 8 and 9, these configurations yield errors of approximately 0.1% with respect to the IGA reference solution. For visualization purposes, the obtained numerical results are smoothed using a Savitzky-Golay filter [65] of order 3 and frame length 13 (Matlab: `sgolayfilt`) to avoid effects introduced by inevitable numerical noise present in the solution.

[3] Remark: Sensor holes are infinitesimally small virtual cutouts with circular shape.

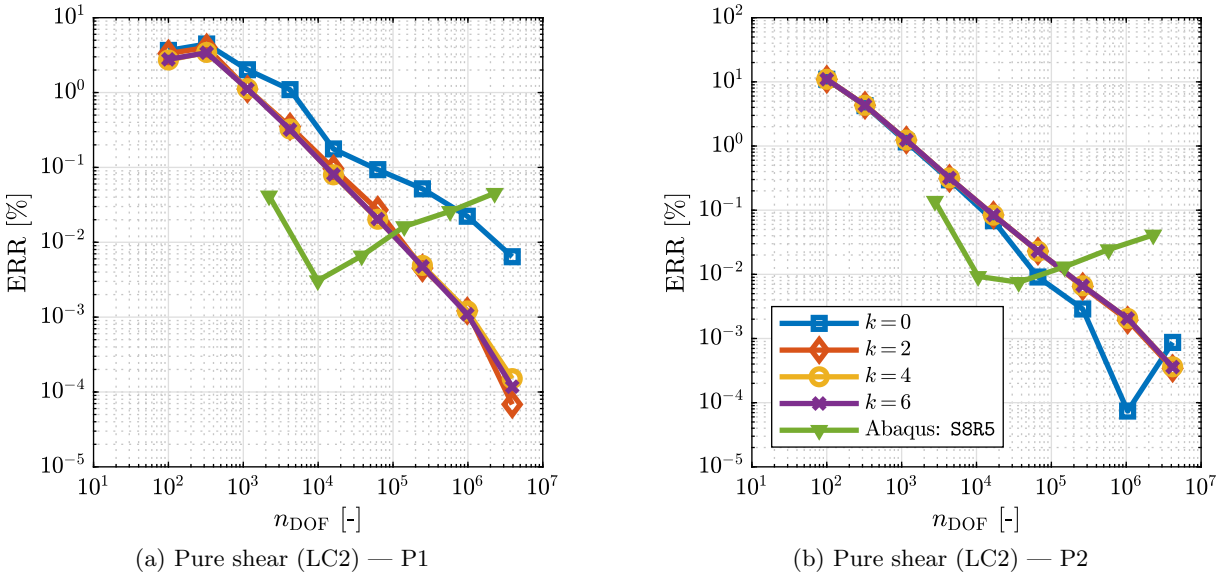


(a) Pure shear (LC2) — P1 (b) Pure shear (LC2) — P2

**Fig. 9.** Error in the critical load for a square plate with a circular cutout under pure shear.

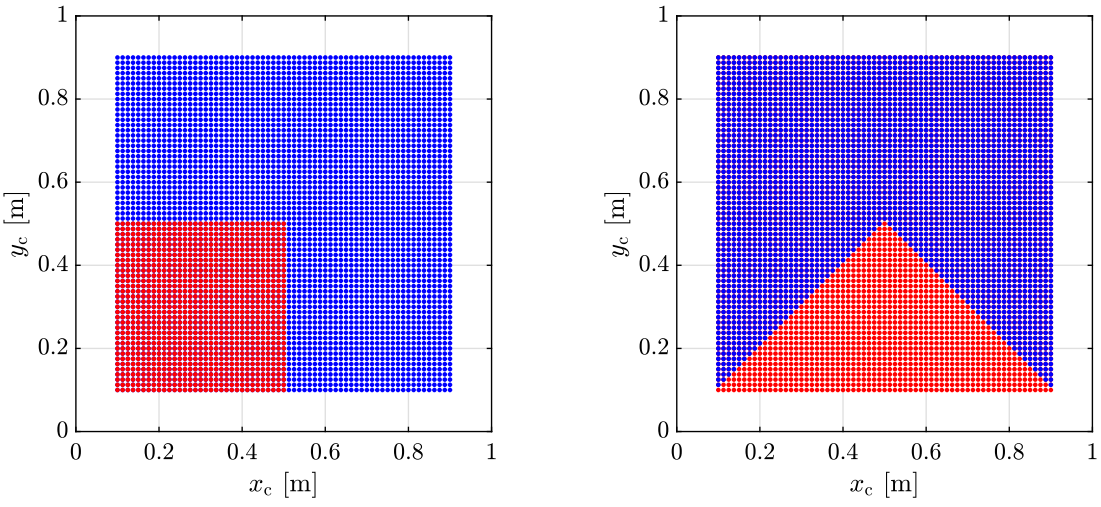


(a) Uniaxial compression (b) Pure shear

**Fig. 10.** Center locations for the numerical analysis of the maximum buckling load of the square plate with circular cutout. Red markers represent the actual simulations that have been executed. The results for the blue markers are obtained by simple transformations (mirroring, rotations).

It is worthwhile to remark that due to the application of a fictitious domain approach, there is no need for expansive re-meshing procedures as the analysis mesh is fixed. In each analysis step, only the identification of cut and fictitious elements must be performed repeatedly, which is a very robust and automated process. Thereafter, the stiffness matrices associated with cut elements are recalculated. Since all uncut elements are of the same shape and have the same material properties, it suffices to compute the elemental matrices for just one finite element and copy the results into the global matrices according to the connectivity/topology data of the spatial discretization.

*6.3.1. Uniaxial compression*

The influence of the position of the circular void on the fundamental buckling load for the uniaxial compression case is depicted in Figs. 11a and c for the different radius values. We clearly observe that there are two regions where an increase in the critical load is caused by introducing a circular hole of radius $r_1$. These regions occur near the edges of the plate where the compression loads are applied. However, the maximum critical load is increased by only 0.76% compared to the buckling load of the intact plate. On the other hand, the reduction in buckling strength is more severe with 4.67%. Also note that in Fig. 11a the position of the circular cutout (marked by an x) for plate P2 has been added. Moreover, the circle drawn with a solid black line indicates the actual size of the cutout for this particular example. As discussed above, we notice that this hole is placed directly in the region with an increased buckling strength. The qualitative behaviour is very similar for the larger void with the radius $r_2$. However, in this case no increase in the buckling strength can be reported. Due to the size of the hole, the decrease in the critical load is between 11.69% and 25.05% compared to the buckling load of the intact plate. Thus, the size of the cutout plays a decisive role in the obtained results. In Fig. 11c, the position of the circular cutout for plate P1 has been shown. The results again confirm the findings reported in Section 6.2.

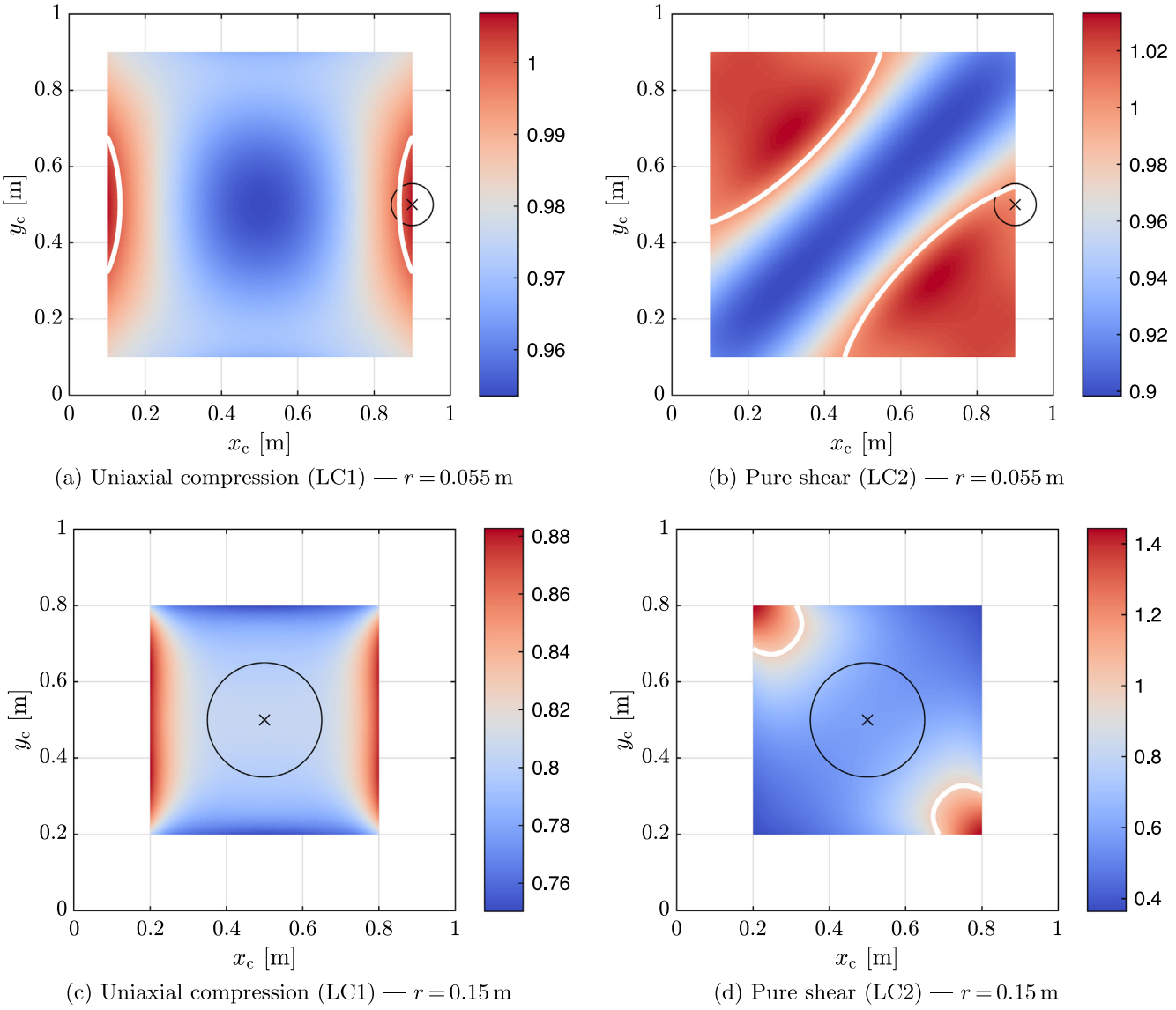


**Fig. 11.** Influence of the position of the center of the circular cutout on the buckling strength. The color scale, displayed in the colorbars, is related to the ratio of the critical loads computed the cut plate and intact plates. The locations and sizes of the cutouts discussed in the previous examples are indicated by an x-marker and a circle drawn in a solid black line.

*6.3.2. Pure shear*

The influence of the position of the circular void on the fundamental buckling load for the pure shear case is depicted in Figs. 11b and d for the different radius values. Again, two distinct regions are observed where an increase in the buckling load is predicted for circular holes of radius $r_1$ or $r_2$. In this example, both the increase but also the decrease in buckling strength are more pronounced compared to the uniaxial compression case. For the first configuration with the smaller hole, an increase of the critical load of up to 3.33% is achieved, while a decrease of up to 10.16% is observed if the hole is incorrectly positioned. Here, the maximum buckling load regions are separated by the diagonal where a decreased load is observed. Interestingly, a larger void region with radius $r_2$ results in much more pronounced variations. For this particular case, increases in the critical load of up to 44.41% are noted, while a significant decrease of 63.76% is also possible. In the pure shear loading case, it is possible to get reasonable results by load reversal. That is to say, while we achieve a "phenomenal" increase in the load, a load reversal will automatically be much more dangerous. This is not seen for the smaller void regions. Considering the uniaxial compression, there is no effect such as that.

The numerical results obtained in this section have shown that a void region does not only lead to a reduction in mass, but can also achieve an increase in the buckling strength of that plate. Even though, the increase might not be very significant depending on the radius of the void, it is helpful to know where cutouts can be placed in a plate if they are required for maintenance or other purposes. This is however, only half the story. We also saw that significant increases are possible for larger voids, but that goes hand in hand with the risk of failure if the loading conditions change. It remains to notice, that the configurations of the domains in Fig. 11, in which the hole must be placed to increase the buckling strength, are qualitatively very similar to those reported in Ref. [7], which have been obtained by means of the "sensor holes" concept. The minor differences are attributed to the finite dimensions of the voids used in our studies.

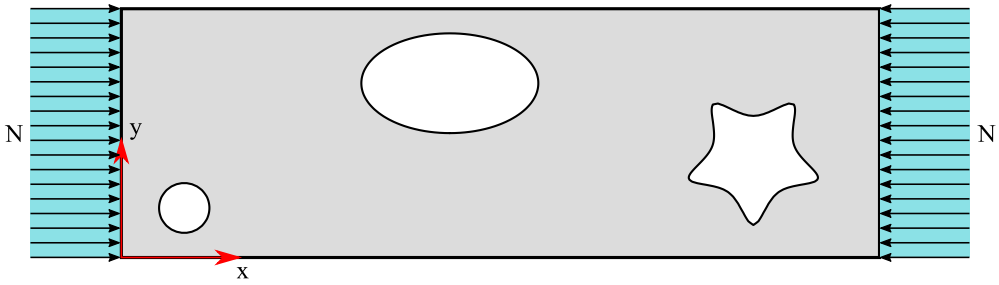


**Fig. 12.** Simply-supported rectangular plate (SSSS) with three cutouts (circle, ellipse, star) subjected to uniaxial compression.

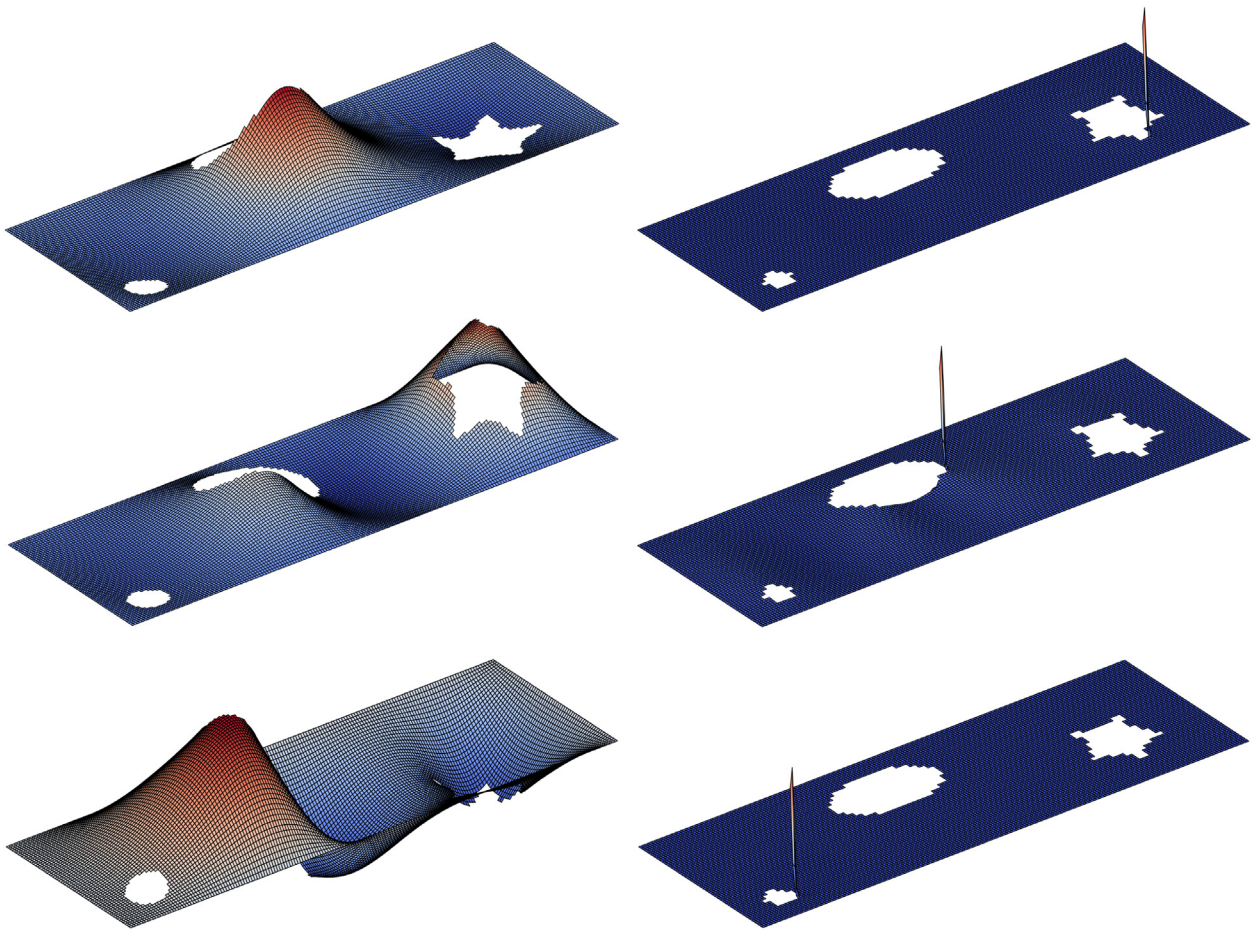

(a) Physical mode shapes (b) Spurious mode shapes

**Fig. 13.** Buckling mode shapes of the simply-supported rectangular plate (SSSS) with three cutouts (circle, ellipse, star) subjected to uniaxial compression. Depicted are the first three physical buckling modes (from top to bottom), which occur at load multiplier values of 508.75, 631.66, and 713.26, respectively. Additionally, three selected spurious modes are shown to illustrate the typical displacement characteristics.

### *6.4. Buckling analysis of a rectangular plate with multiple cutouts*

As a last example, the critical load for a rectangular plate with multiple cutouts is computed. This example serves to demonstrate that the proposed method is also applicable to geometrically more complex structures, where the mesh generation would be very involved for numerical methods requiring a geometry-conforming discretization. Thus, the example serves to demonstrate the advantages of an automatic approach compared to methods that rely on user intervention and expertise in mesh generation. The dimensions of the plate are $l_x = 3$ m, $l_y = 1$ m, and $t = 1$ mm (see Fig. 12). Note that the kinematic boundary conditions are identical to those used in the previous examples. Three different cutouts are introduced in the plate and the corresponding level-set functions (to determine whether points are located within the fictitious or physical domain) are given below:

1. Circular cutout: $r = 0.1$ m, $x_c = 0.25$ m, and $y_c = 0.2$ m

$$\mathfrak{L}_{\text{circ}}(\mathbf{x}) = (x - x_c)^2 + (y - y_c)^2 - r^2. \tag{35}$$

2. Elliptical cutout: $a = 0.35$ m, $b = 0.2$ m, $x_c = 1.3$ m, and $y_c = 0.7$ m

$$\mathfrak{Q}_{\text{ellipse}}(\mathbf{x}) = \frac{(x-x_c)^2}{a^2} + \frac{(y-y_c)^2}{b^2} - 1. \tag{36}$$

3. Star-shaped cutout: $a = 35, b = 1.25, x_c = 2.5$ m, and $y_c = 0.4$ m

$$\begin{aligned} &\mathfrak{Q}_{\text{star}}(\mathbf{x}) = \sqrt{a(x-x_c)^2 + a(y-y_c)^2} - r(x,y), \quad \text{with} \\ &r(x,y) = \left[\cos^{10}(b\theta(x,y)) + \sin^{10}(b\theta(x,y))\right]^{-1/6}, \\ &\theta(x,y) = \texttt{atan2}(x-x_c, y-y_c). \end{aligned} \tag{37}$$

The mathematical function `atan2` in (37) denotes the four-quadrant inverse tangent of the argument $\chi = x - x_0/y - y_0$. The plate and the selected void regions are displayed in Fig. 12. The fundamental buckling load is only calculated for the case of a uniaxial compression (LC1).

Again, the analytical solution for buckling loads of different orders, i.e., buckling loads with more than one sine-half wave in one of the plate directions or in other words higher eigenvalues of the generalized eigenvalue problem presented in (23), can be calculated by means of (32). This is the reference solution for an intact rectangular plate. The fundamental buckling load is obtained for $m = 3$ and $n = 1$, i.e., for three half-waves in $x$- and one in $y$-direction. This yields a value of the load multiplier of 759.2, which is identical to the square plate case. Considering the simply-supported plate with multiple cutouts a value of the load multiplier of 508.75 is achieved (without applying any of the introduced filtering techniques[4]), which is significantly lower than the analytical reference value. The numerical result has been computed utilizing a spatial discretization consisting of $n_e^x = 96$ elements in $x$-direction and $n_e^y = 32$ elements in $y$-direction, while the refinement level for the subcell integration scheme is $k = 2$. This is all too natural, since the cutouts are comparably large and make up $0.385\,\text{m}^2$, which is roughly 13% of the area of the intact plate. Thus, the void region for this final example is considerably larger than in the previous problems. Therefore, a more drastic decrease in the buckling is also expected. In Fig. 13, the selected mode shapes of physical and spurious buckling modes are depicted.

## 7. Summary

In the paper at hand, a cut BFS element for the analysis of buckling problems has been developed. The original BFS element is arguably one of the simplest element formulations that ensures $C^1$-continuity between adjacent elements and yet achieves very accurate results. This remarkable accuracy is based on the bicubic Hermitian polynomials being used as shape functions. Its only shortcoming is seen in the need for a structured (regular) discretization and therefore, BFS elements are not widely applied in industrial practice. This shortcoming has been fixed by combining the original element with a fictitious domain approach, yielding cut BFS elements. As fictitious domain methods are exclusively relying on Cartesian meshes, the problem of conventional BFS elements becomes a feature of cut BFS elements. By means of several numerical examples, it has been conclusively shown that despite the simple formulation of the novel cut BFS elements very accurate results are obtained.

[4] Remark: By treating all cut elements as either fictitious elements (discarded from the analysis) or finite elements (physical boundary within the element is disregarded), one can obtain a lower and an upper bound for the correct buckling load. Thus, the correct value for the load multiplier can be selected from among the spurious solutions. For this particular example, employing the filtering technique 3 (see Appendix A) would result in a load multiplier of 501.3 ($A^e_{\text{del}} = 0.1\%$), which incurs an error of approximately 1.5%. Even if we increase the value of $A^e_{\text{del}}$ to 0.8% the resulting error is still below 2% compared to the unfiltered solution.

## 8. Conclusion

The analysis of the critical buckling load of plates with cutouts has led to the following conclusions: Depending on the size of the introduced void region, an increase in the buckling load can still be achieved. This behavior is surprisingly more pronounced for a larger void, however, this goes along with the risk of a significant reduction of the critical load for other loading directions.

A problem that needs to be overcome when applying fictitious domain approaches for the analysis of eigenvalue problems is the occurrence of spurious modes, which are not always easy to identify or to distinguish from physical modes. One of the main characteristics of the FCM as a particular approach to fictitious domain methods is that the displacement field is allowed to extend smoothly into the fictitious domain. This is one source for the occurrence of local buckling modes that originate in the fictitious domain. These modes need to be suppressed without changing the mathematical problem at hand to ensure a robust methodology. This is an important aspect of further research.

Another potential application of the discussed technique would be the analysis of axially moving plate and shell structures with cuts using the mixed Eulerian–Lagrangian kinematic description, see e.g., Ref. [66]. While the cuts are moving across the non-material finite element mesh, they shall be captured by means of the presented fictitious domain approach. This provides a way towards efficient simulations of such technological processes as roll forming of profiles of perforated steel sheets or transport of flat structures with holes. Embedding the fictitious domain approach into the structural mechanics formulations with contact and material inelasticity shall be considered as a challenging but practically relevant novel research direction.

## Declaration of Competing Interest

The authors declare that they have no known competing financial interests or personal relationships that could have appeared to influence the work reported in this paper.

## Acknowledgements

The authors gratefully acknowledge the insightful discussions and helpful comments provided by Prof. Dr.-Ing. habil. Martin Ruess (University of Applied Sciences Düsseldorf) and Priv.-Doz. Dr.-Ing. habil. Stefan Kollmannsberger (Technical University of Munich) regarding the numerical problems encountered when solving eigenvalue problems in the context of fictitious domain methods. J. Kiendl was partially supported by the European Research Council (ERC) under the European Union's Horizon 2020 research and innovation program (grant agreement No 864482). This support is gratefully acknowledged.

## Appendix A. Filtering techniques

The need of filtering is related to the occurrence of spurious buckling modes (i.e., local buckling modes partly located in the fictitious domain). In preliminary analysis, it has been found that the conditioning of the system of equations does not provide reliable information to indicate the occurrence of spurious results. Moreover, it must be noted that sometimes despite the existence of very badly cut elements in the spatial discretization accurate results are obtained, while in other less severe cases corrupted results are obtained. Therefore, additional research must be conducted to ascertain the actual cause of these numerical problems. Although it has been found that the filtering techniques proposed in the remainder of this section work quite robustly in detecting non-

physical results, they do not solve the inherent problem that causes this effect.

In the following, several possibilities are discussed, which have been implemented in the in-house research code (developed in MATLAB) that is used for the numerical analysis. The suggested methods are referred to as:

1. Displacement-based mode shape filtering,
2. Strain energy-based mode shape filtering,
3. Area-based element filtering,
4. Support-based degree of freedom filtering.

### A.1. Mode shape-based filtering techniques

The first and second filtering techniques are based on the variation of the computed displacement field for a buckling mode. The main goal is to identify common features for all spurious mode shapes and to exploit these features to robustly detect them.

*Displacement-based mode shape filtering.* Let us start with taking a closer look at the displacement fields of physical and spurious buckling mode shapes as depicted in Fig. A.1 for plate P1 (see Section 6.2). For the purpose of visualization, all elements including cut elements have been plotted, which means that the displacement field within the fictitious domain is also shown. It can be clearly observed that displacement peaks are present in the fictitious domain, which is related to the fact that the displacement field is allowed to smoothly extend beyond the physical domain. This is actually no problem, but ensures the proven high accuracy of the FCM. However, what is problematic is that the displacement values in the fictitious domain are much larger than in the physical domain for the spurious modes, while they are in the same order of magnitude for the physical ones. This observation can be used as the basis for deriving a first displacement-based filtering technique. In the following, we assume without loss of generality that all computed mode shapes are normalized such that the maximum displacement is $+1$. In the next step, we determine all nodes of the mesh that are located in the physical domain (the rest of the nodes is then naturally part of the fictitious domain). To this end, a simple point-membership-test is conducted, which is particularly simple if level-set (or implicit) functions are utilized to describe the geometry of the fictitious domain. Thus, we can subdivide the set of nodes $\mathscr{P}$ into $\mathscr{P}_{\text{phys}}$ and $\mathscr{P}_{\text{fict}}$, with $\mathscr{P}_{\text{phys}} \cup \mathscr{P}_{\text{fict}} = \mathscr{P}$ and $\mathscr{P}_{\text{phys}} \cap \mathscr{P}_{\text{fict}} = \varnothing$. From the connectivity data of the finite element discretization, we only need to extract the displacement degrees of freedom of each of the nodes in those two sets, denoted by $\mathscr{D}_{\text{phys}}$ and $\mathscr{D}_{\text{fict}}$. The ratio of the maximum displacement values

$$R_{\text{w}} = \frac{\max[w(\mathscr{D}_{\text{fict}})]}{\max[w(\mathscr{D}_{\text{phys}})]} \tag{A.1}$$

will then be used to judge the mode. If the ratio is above 10, the mode is marked as nonphysical. Note that this value is empirical and not a strict bound and therefore, false classifications might occur. To prevent this from happening, a combination with the second filter, described in the next paragraph, is recommended. This

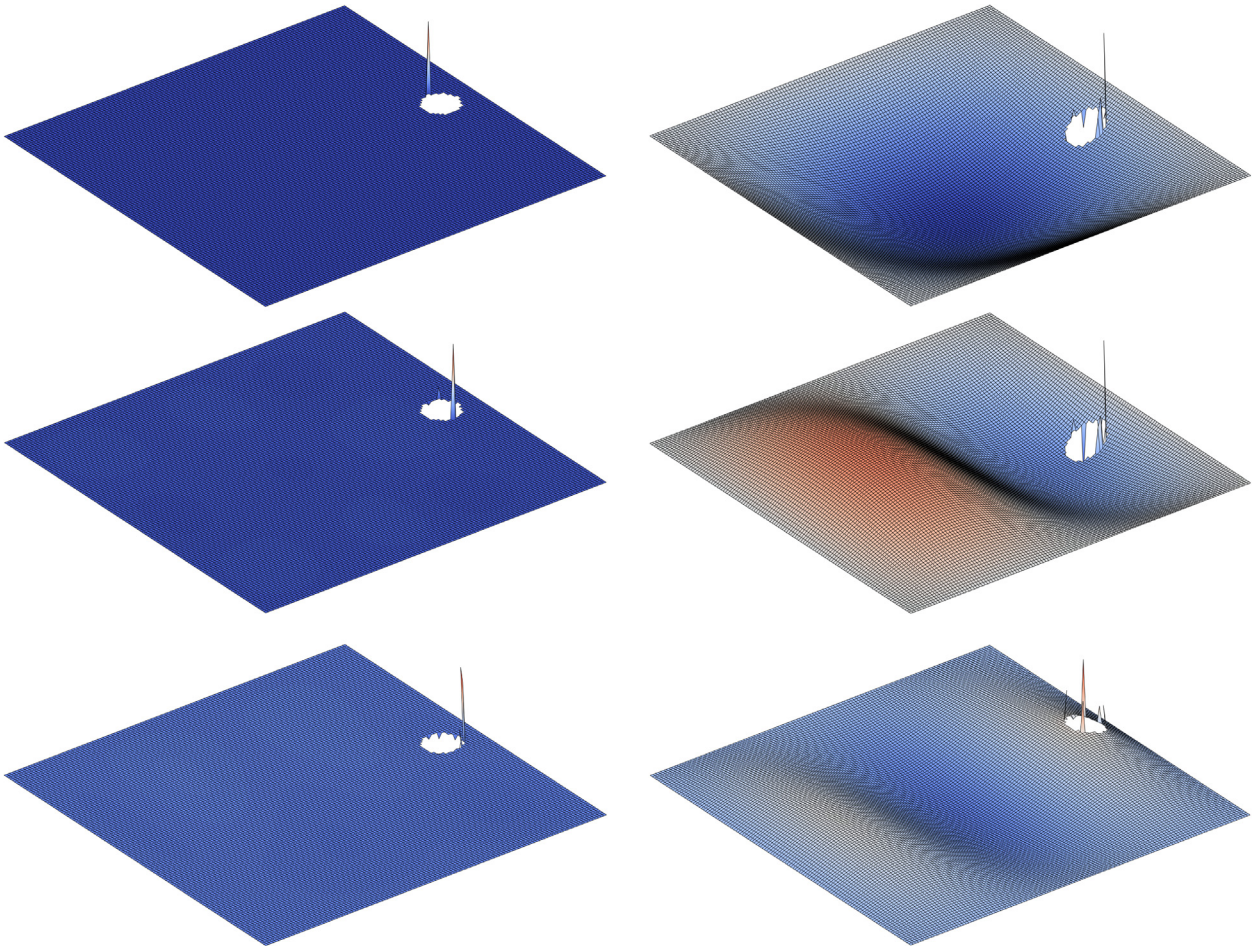

(a) Spurious buckling modes (b) Physical buckling modes

**Fig. A.1.** Mode shapes for a simply-supported (SSSS) square plate with a circular cutout (P2; LC1).

procedure allows for a robust classification of the results of the eigenvalue analysis.

*Strain energy-based mode shape filtering.* A second idea, also inspired by the excessive displacements in the fictitious domain for spurious mode shapes (see Fig. A.1), consists in computing the strain energy for all degrees of freedom associated with the sets of nodes $\mathscr{P}_{\text{phys}}$ and $\mathscr{P}_{\text{fict}}$. To determine the energy value, we take all four degrees of freedom per node into account. This is different compared to the displacement-based filtering technique, described in the previous paragraph, where only the displacement degrees of freedom have been accounted for. Consequently, the new sets of degrees of freedom that are employed in the strain energy-based filtering technique are denoted as $\tilde{\mathscr{P}}_{\text{phys}}$ and $\tilde{\mathscr{P}}_{\text{fict}}$. According to (13), the strain energy is computed as

$$U^{\text{b}}_{\text{phys}} = \frac{1}{2} q^T_{\text{phys}} K q_{\text{phys}}, \quad \text{with } q_{\text{phys}}\left(\tilde{\mathscr{P}}_{\text{phys}}\right) = q\left(\tilde{\mathscr{P}}_{\text{phys}}\right) \text{and } q_{\text{phys}}\left(\tilde{\mathscr{P}}_{\text{fict}}\right) = 0, \tag{A.2}$$

$$U^{\text{b}}_{\text{fict}} = \frac{1}{2} q^T_{\text{fict}} K q_{\text{fict}}, \quad \text{with } q_{\text{fict}}\left(\tilde{\mathscr{P}}_{\text{fict}}\right) = q\left(\tilde{\mathscr{P}}_{\text{fict}}\right) \quad \text{and } q_{\text{fict}}\left(\tilde{\mathscr{P}}_{\text{phys}}\right) = 0. \tag{A.3}$$

We recall that $K$ denotes the stiffness matrix of the plate bending problem and $q$ is the vector of degrees of freedom associated with a particular buckling mode. As can be inferred from the equations, all values that are not related to the physical or fictitious parts are set to zero for the calculation of the corresponding energies. In order to decide whether a buckling mode is nonphysical, the ratio of the two strain energies is determined

$$R_{\text{SE}} = \frac{U^{\text{b}}_{\text{fict}}}{U^{\text{b}}_{\text{phys}}}. \tag{A.4}$$

Values above 1.0 are deemed nonphysical and therefore, the mode would be marked as spurious. Judging from our experience, if both criteria, i.e., the displacement- and strain energy-based filtering techniques, mark/label a buckling mode as nonphysical the classification result is rather reliable.

### A.2. Element-based filtering techniques

The third and fourth filtering techniques are based on the properties of the spatial discretization and are thus, not connected to the buckling modes directly. Here, the overarching goal is to identify badly cut elements or shape functions that do not contribute much to the system of equations.

*Area-based element filtering.* Based on an area-filter, cut elements are identified, which are critical for the numerical stability of the solution, and are discarded. To this end, the total and physical areas of each cut BFS element are computed

$$A^{\text{tot}}_{\text{e}} = \int_{\Omega_{\text{e}}} \mathrm{d}\Omega = h_{\text{x}} h_{\text{y}}, \quad A^{\text{phys}}_{\text{e}} = \int_{\Omega_{\text{e}}} \alpha(\mathbf{x}) \mathrm{d}\Omega,$$
$$A^{\text{void}} = \int_{\Omega_{\text{e}}} (1 - \alpha(\mathbf{x})) \mathrm{d}\Omega = A^{\text{tot}}_{\text{e}} - A^{\text{phys}}_{\text{e}}, \tag{A.5}$$

where $h_i$ are the element sizes in the respective coordinate directions and $\Omega_{\text{e}}$ represents the integration domain of an element. Note that the subscript $\square_{\text{e}}$ always refers to elemental entities. The ratio of physical to total area is called $\chi_{\text{A}}$, which should be below a user-defined threshold $A^{\text{thr}}$ for the element to discarded. This value is chosen adaptively depending on the three area measures $A^{\text{tot}}_{\text{e}}, A^{\text{phys}}_{\text{e}}$, and $A^{\text{void}}$ introduced in (A.5):

$$A^{\text{thr}} = \frac{A^{\text{void}}}{A^{\text{tot}}_{\text{e}}} A^{\text{del}}_{\text{e}} \,[\%] < \chi_{\text{A}} = \frac{A^{\text{phys}}_{\text{e}}}{A^{\text{tot}}_{\text{e}}}, \tag{A.6}$$

with $A^{\text{del}}_{\text{e}}$ denoting the area of the void region in percent. That is to say, a cut BFS element might be discarded from the analysis as soon as the physical area it contributes to the model $A^{\text{phys}}$ is less than $A^{\text{del}}_{\text{e}}/100 A^{\text{void}}$. For example, if $A^{\text{del}}_{\text{e}} = 0.1\%$, one cut element is allowed to contain $0.1\%$ of $A^{\text{void}}$ and can still be deleted from the analysis. This value is obviously directly related to the achievable accuracy of the approach. Since the area of the void in the model is constant throughout the analysis the value of $A^{\text{thr}}$ increases with decreasing element size. For the studied examples, $A^{\text{del}}_{\text{e}} = 0.1\%$ and $A^{\text{thr}} < 50\%$ has been shown to yield reliable results within an engineering accuracy of around $\pm 1\%$. To put the selected parameter values into perspective, it means that when the maximum value of $50\%$ is reached, 200 elements are covering the same area as the void, which constitutes a very fine spatial discretization that is hardly needed for any analysis (especially considering the fact that the BFS shape functions are bi-cubic already). Note that the need for a filter typically only arises for rather fine spatial discretizations and high order modes. For the examples discussed in Section 6.2 (square plate with circular cutout), the filter is typically required for $n_{\text{e}} \geqslant 16$ elements per coordinate direction if the value for $\alpha_0$ is chosen too small.

*Support-based degree of freedom filtering.* Based on a degree of freedom-filter, degrees of freedom with small support in the physical domain are identified, which are critical for the numerical stability of the solution, and are discarded. This can be achieved by integrating each shape function both over the cut element and the entire elemental domain. By dividing both values we get a relative measure $\iota_{\text{supp}}$ of the support of a function

$$\iota^{i,j}_{\text{supp}} = \frac{\int_{\Omega^{\text{e}}} \alpha(\mathbf{x}) S_{i,j}(\xi) \mathrm{d}\Omega}{\int_{\Omega^{\text{e}}} S_{i,j}(\xi) \mathrm{d}\Omega} < \iota^{\text{thr}}_{\text{supp}}, \tag{A.7}$$

where $S_{i,j}$ denotes the $j$th shape function of node $i$ (see Section 2). The threshold for shape functions to be deleted is by default set to $\iota^{\text{thr}}_{\text{supp}} = 10^{-5}$. In combination with the area-based filtering technique, the support-based one is rarely ever applied. On its own, it does not seem to be effective enough to alleviate the spurious modes problem.

### A.3. Concluding remark on the different filtering techniques

At this point, we want to stress again that none of the filtering techniques are required to accurately determine the first buckling mode. In this case, it is sufficient to rely on (30) for an appropriate choice of $\alpha$. However, if higher order modes are of interest, filtering techniques need to be applied. From experience, the combined use of approaches 1 and 2 is recommended. Note that by using approaches 3 and 4, the system/problem under investigation is essentially changed and therefore, great care has to be taken to ensure that the results are still reasonable. Despite the mentioned shortcomings, these approaches seem to work robustly and ensure reliable results. It must be emphasized that the proposed methods are also applicable to the problem of *Modal Analysis*, where an eigenvalue problem is solved to determine the natural frequencies and mode shapes. However, since these techniques are neither mathematically elegant nor based on a solid theoretical foundation, more sophisticated techniques should be developed in future research.

## Appendix B. $C^1$-continuous NURBS parametrization of a square plate with a circular cutout

This section contains the details of the geometry parametrization of a square plate with a circular cutout by an untrimmed, fully $C^1$-continuous, single NURBS patch, which is the basis of the IGA computations performed in Section 6. Due to the cutout, a simple parametrization with parametric coordinates aligned with the sides of the plate is not possible without trimming. Instead, the

geometry can be modeled as a swept area between the outer and inner boundaries. In this case, the four corners pose the difficulty of having sharp corners within a $C^1$-continuous, i.e., smooth, parametrization. This problem can be solved by collapsing control points at the corners, as was shown in Ref. [45] for a quarter of such a plate.

In the following, we describe a general procedure to model the geometry of a square plate of dimension $a$ with a circular cutout at an arbitrary location $(x_c, y_c)$ with a radius $r$ via a single, fully $C^1$-continuous NURBS patch. This methodology is based on three steps, which are illustrated in Fig. B.1 and discussed in detail in the following paragraphs.

We start by modeling a circular disk with a circular cutout, where the diameter of the outer circle is equal to the square's dimension $a$. Table B.1 lists the NURBS parameters for such a geometry, where $p$ and $q$ denote the polynomial degrees in the two parametric directions, where first coincides with the circumferential direction and the second with the radial one. The corresponding knot vectors are denoted by $U$ and $V$, respectively. Control point coordinates are denoted as $X_o, Y_o$ and $X_i, Y_i$ for the outer and inner control points, respectively, while the control weights $W$ are identical for both the outer and inner control points. The parametrization given in Table B.1 is defined in terms of the parameters $a, x_c, y_c$, and $r$, such that it allows for arbitrary variations of the cutout within the plate. Fig. B.1a depicts the corresponding geometry and control net for $a = 1$ m, $x_c = y_c = 0.5$ m, $r = 0.15$ m.

As a second step, each knot span in $U$ is bisected, i.e., additional knots are inserted at $1/8, 3/8, 5/8, 7/8$, in order to obtain additional control points as shown in Fig. B.1b.

In the third step, control point coordinates are edited such that the two points closest to each corner of the square are moved to that corner, see Fig. B.1c. The coincidence of two control points leads to sharp corners without losing $C^1$-continuity of the parametrization within the patch. The model obtained in such a way represents the coarsest mesh of the geometry. For analysis, it can then be further refined using order elevation and knot insertion [45]. For the buckling analysis reference results in Section 6, the polynomial degrees are set to $p = q = 6$ and a mesh corresponding to 220,698 degrees of freedom was used. For the static analysis reference results in Section C, the polynomial degrees are set to $p = q = 6$ and a mesh corresponding to 61,530 degrees of freedom was used.

*Remark 1:* The initial parametrization provided in Table B.1 contains four lines of $C^0$-continuity in the parametric space due to double knots in the knot vector $U$. The physical image of these lines are the four knot lines at 6, 3, 12, and 9 o'clock. $C^1$-continuity of the geometry is given because of the colinearity of control points across these lines [25]. $C^1$-continuity of the solution can be imposed by enforcing the colinearity of these control points also in the deformed configuration, which is done by master–slave constraints as described in Ref. [25].

**Table B.1**
NURBS parametrization of a circular disk with a circular cutout. The outer radius of the disk is $a/2$ and its center is located at $x = y = a/2$. The cutout may have an arbitrary location described by its center coordinates $x_c, y_c$ and a radius $r$.

| Parameter | Value |
|---|---|
| $p$ | 2 |
| $q$ | 1 |
| $U$ | [0, 0, 0, 1/4, 1/4, 1/2, 1/2, 3/4, 3/4, 1, 1, 1] |
| $V$ | [0, 0, 1, 1] |
| $X_o$ | [1, 2, 2, 2, 1, 0, 0, 0, 1] $a/2$ |
| $Y_o$ | [0, 0, 1, 2, 2, 2, 1, 0, 0] $a/2$ |
| $X_i$ | [0, 1, 1, 1, 0, −1, −1, −1, 0] $r + x_c$ |
| $Y_i$ | [−1, −1, 0, 1, 1, 1, 0, −1, −1] $r + y_c$ |
| $W$ | $\left[1, \sqrt{1/2}, 1, \sqrt{1/2}, 1, \sqrt{1/2}, 1, \sqrt{1/2}, 1\right]$ |

*Remark 2:* For obtaining a fully $C^1$-continuous parametrization, it is important that the outer boundary of the initial geometry (Fig. B.1a) is modeled as an exact circle, i.e., using the weights $W$, although this boundary is then modified to represent a square. If this is not the case, e.g., if all weights of the outer control points are simply set to 1, the resulting geometry will still be a square plate with a circular cutout (Fig. B.1c), but it will not be $C^1$-continuous at the 6, 3, 12, 9 o'clock locations.

## Appendix C. Static analysis

In the following, the performance of the proposed cut BFS elements for plate bending problems is briefly discussed. While in the present article, a combination of FCM and BFS elements is presented, the main features of this formulation are shared by the cut BFS elements discussed in Ref. [6] for static analysis. In the mentioned article, BFS elements were enhanced by utilizing the CutFEM approach, which also belongs to the class of fictitious domain methods. The authors were able to show that the elements are optimally order convergent and stable. These properties are expected to seamlessly carry over to our formulation. Therefore, we will only demonstrate the convergence of the proposed element type by means of a simple static example featuring a simply-supported plate with a circular cutout under a uniform surface load. In fact, the geometry and kinematic boundary conditions

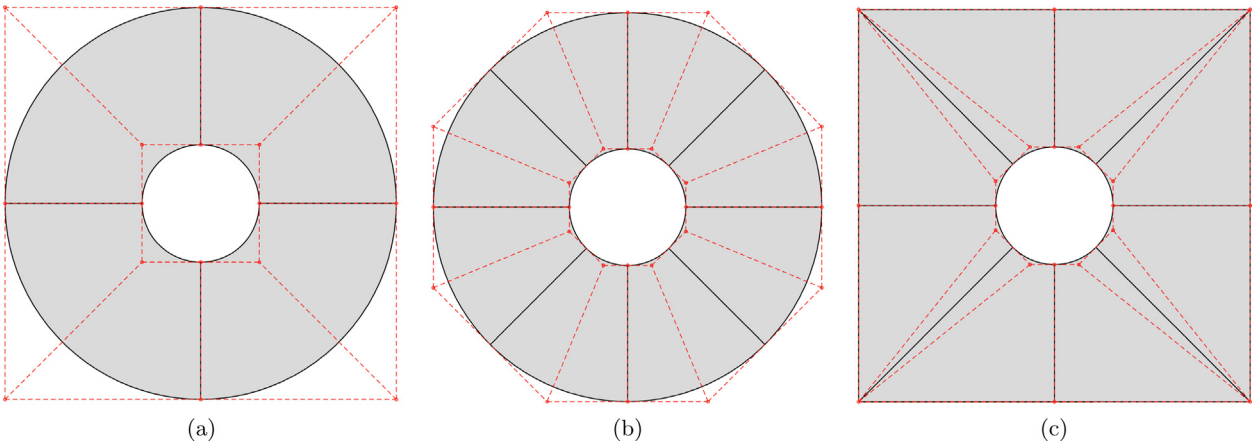


**Fig. B.1.** NURBS parametrization of a square with a circular cutout. Construction in three steps.

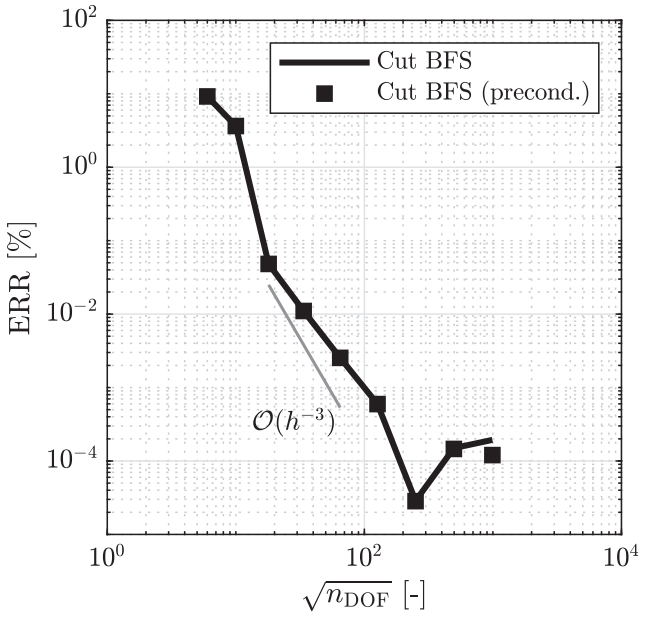


**Fig. C.1.** Convergence in strain energy for a simply supported plate with circular cutout under uniform surface load.

are identical to those given for plate (P1), studied in Section 6.2. To ensure an accurate approximation of the cutout during the integration of the stiffness matrix and the load vector, the refinement level $k$ is set to 4. The convergence in the strain energy is depicted in Fig. C.1, where the reference solution is computed again using an IGA model as discussed in Section B and is obtained as $U^{\mathrm{b}} = 4.1176963 \times 10^{-5}$ J. We observe a monotonic convergence of the strain energy with an optimal order $\mathcal{O}\left(h^{-3}\right)$. In contrast to the generalized eigenvalue problem that is solved for the buckling analysis, the solution of linear systems of equations is not as susceptible to suffer from small cuts, i.e., elements that hardly contain physical material. Therefore, the simplified (diagonal) preconditioning technique as proposed by de Prenter et al. [10] can be applied to this problem and yields notably improved condition numbers for the stiffness matrix (see Table C.2). Note that all values that are related to the preconditioned system are denoted with $\tilde{\square}$, where $U^{\mathrm{b}}$ denotes the strain energy associated to plate bending and $\kappa$ is the condition number of the stiffness matrix. In the case of generalized eigenvalue problems, it has been found that the simple diagonal preconditioning approach is not sufficient to overcome ill-conditioning and more importantly the spurious mode shapes problem. Consequently, the complete preconditioning scheme must be employed, which is, however, out of the scope of this article. At this point, we must stress again that even without applying any preconditioning technique the results of the static analysis are very accurate. That is to say, in analyses involving the solution of eigenvalue problems different techniques are required compared to static analyses.

**Table C.2**
Results of the static plate bending problem.

| $n_{\mathrm{DOF}}$ | $U^{\mathrm{b}}$ | $\tilde{U}^{\mathrm{b}}$ | $\kappa$ | $\tilde{\kappa}$ |
|---|---|---|---|---|
| 36 | 3.738898E-5 | 3.738898E-5 | 73.755 | 17.441 |
| 100 | 3.967871E-5 | 3.967871E-5 | 414.285 | 311.102 |
| 324 | 4.115711E-5 | 4.115711E-5 | 2.143E4 | 4.793E3 |
| 1,136 | 4.117242E-5 | 4.117242E-5 | 3.172E7 | 1.405E5 |
| 4,208 | 4.117592E-5 | 4.117592E-5 | 1.162E11 | 1.508E7 |
| 16,016 | 4.117721E-5 | 4.117721E-5 | 2.457E9 | 2.190E7 |
| 62,560 | 4.117695E-5 | 4.117695E-5 | 4.250E12 | 3.857E8 |
| 246,864 | 4.117690E-5 | 4.117690E-5 | 3.014E12 | 6.214E9 |
| 981,056 | 4.117688E-5 | 4.117691E-5 | 2.974E12 | 9.490E10 |

For the sake of completeness, let us briefly recall the diagonal preconditioning scheme discussed in Ref. [10]. It has been shown that this approach works well for Poisson and linear elasticity problems, being able to efficiently reduce the condition number of the system matrix. This method is, however, not recommended for general use due to fill-in and a lack of robustness for arbitrarily cut elements. For a generic linear system of equations

$$\mathbf{A}\mathbf{x} = \mathbf{b}, \tag{C.1}$$

a symmetry preserving preconditioning technique takes the following form

$$\mathbf{D}\mathbf{A}\mathbf{D}^{\mathrm{T}}\mathbf{y} = \mathbf{D}\mathbf{b}, \qquad \text{with} \quad \mathbf{x} = \mathbf{D}^{\mathrm{T}}\mathbf{y}. \tag{C.2}$$

In this framework, $\mathbf{D}$ denotes the diagonal preconditioner and $\mathbf{y}$ is the solution to the preconditioned linear system of equations. The solution to the original system $\mathbf{x}$ is obtained in simple post-processing step by left-multiplying the transpose of the preconditioner $\mathbf{D}^{\mathrm{T}}$ to the solution $\mathbf{y}$. For our purposes, the diagonal preconditioner is defined as

$$\mathbf{D} = \begin{bmatrix} 1/\sqrt{A_{11}} & & & \\ & 1/\sqrt{A_{22}} & & \\ & & \ddots & \\ & & & 1/\sqrt{A_{NN}} \end{bmatrix}, \tag{C.3}$$

where $N$ denotes the size of the system matrix $\mathbf{A}$. As indicated before, a reasonable improvement of the conditioning of the stiffness matrix is achieved, while the accuracy of the results (considering the converged digits) is not changed at all, as evidenced by Table C.2.

## References


[1] Bogner FK, Fox RL, Schmit LA. The generation of interelement compatible stiffness and mass matrices by the use of interpolation formulae. In: Proceedings of the 1st conference on matrix methods in structural mechanics; 1965. p. 397–444.

[2] Vetyukov Y. Finite element modeling of Kirchhoff-Love shells as smooth material surfaces. ZAMM 2014;94(1–2):150–63. https://doi.org/10.1002/zamm.201200179.

[3] Parvizian J, Düster A, Rank E. Finite cell method: h- and p-extension for embedded domain problems in solid mechanics. Comput Mech 2007;41:121–33. https://doi.org/10.1007/s00466-007-0173-y.

[4] Düster A, Rank E, Szabó B. The p-Version of the Finite Element and Finite Cell Methods, John Wiley & Sons; 2018, Ch. 4. p. 1–55. doi:10.1002/0470091355.

[5] Duy R. Fictitious domain approach for optimizing stability boundaries of plates with cutouts, Master's thesis, Vienna University of Technology; 2021. doi:10.34726/hss.2021.70501.

[6] Burman E, Hansbo P, Larson MG. Cut Bogner-Fox-Schmit elements for plates. Adv Model Simul Eng Sci 2020;7(1):1–20. https://doi.org/10.1186/s40323-020-00164-3.

[7] Gracia JB, Rammerstorfer FG. Increase in buckling loads of plates by introduction of cutouts. Acta Mech 2019;230(8):2873–89. https://doi.org/10.1007/s00707-019-02435-6.

[8] Zienkiewicz OC, Taylor RL. The Finite Element Method – Volume 2: Solid Mechanics, Butterworth Heinemann; 2000.

[9] Vetyukov Y. Nonlinear Mechanics of Thin-Walled Structures. Asymptotics, Direct Approach and Numerical Analysis, Foundations of Engineering Mechanics, Springer, Vienna; 2014. doi:10.1007/978-3-7091-1777-4.

[10] de Prenter F, Verhoosel CV, van Zwieten GJ, van Brummelen EH. Condition number analysis and preconditioning of the finite cell method. Comput Methods Appl Mech Eng 2017;316:297–327. https://doi.org/10.1016/j.cma.2016.07.006.

[11] de Prenter F, Verhoosel CV, van Brummelen EH, Evans JA, Messe C, Benzaken J, Maute K. Multigrid solvers for immersed finite element methods and immersed isogeometric analysis. Comput Mech. doi:10.1007/s00466-019-01796-y.

[12] Burman E, Hansbo P. Fictitious domain finite element methods using cut element: II. A stabilized Nitsche method. Appl Numer Math 2012;62:328–41. https://doi.org/10.1016/j.apnum.2011.01.008.

[13] Reissner E. On the theory of transverse bending of elastic plates. Int J Solids Struct 1976;12(8):545–54. https://doi.org/10.1016/0020-7683(76)90001-9.

[14] Elishakoff I. Handbook on Timoshenko–Ehrenfest beam and Uflyand–Mindlin plate theories, World Scientific; 2020. doi:10.1142/9789813236523_0002.

[15] Brezzi F, Bathe K-J, Fortin M. Mixed-interpolated elements for Reissner-Mindlin plates. Int J Numer Meth Eng 1989;28(8):1787–801. https://doi.org/10.1002/nme.1620280806.

[16] Durán R, Liberman E. On mixed finite element methods for the Reissner-Mindlin plate model. Math Comput 1992;58(198):561–73. https://doi.org/10.1090/S0025-5718-1992-1106965-0.

[17] Batoz J, Bathe K, Ho L. A study of three-node triangular plate bending elements. Int J Numer Meth Eng 1980;15:1771–821. https://doi.org/10.1002/nme.1620151205.

[18] Dassault Systemes Simulia Corp., Providence, RI, USA, ABAQUS Theory Manual, vol 6.6, section 3.6.4; 2009. https://classes.engineering.wustl.edu/2009/spring/mase5513/abaqus/docs/v6.6/books/stm/ch03s06ath82.html.

[19] Noels L. A discontinuous Galerkin formulation of non-linear Kirchhoff-Love shells. Int J Numer Meth Eng 2009;78:296–323. https://doi.org/10.1002/nme.2489.

[20] Ludwig T, Hühne C, De Lorenzis L. Rotation-free Bernstein-Bézier elements for thin plates and shells–development and validation. Comput Methods Appl Mech Eng 2019;348:500–34. https://doi.org/10.1016/j.cma.2019.01.039.

[21] Dufva K, Shabana A. Analysis of thin plate structure using the absolute nodal coordinate formulation. IMechE J Multi-body Dynam 2005;219:345–55. https://doi.org/10.1243/146441905X50678.

[22] Schwab AL, Gerstmayr J, Meijaard JP. Comparison of three-dimensional flexible thin plate elements for multibody dynamic analysis: finite element formulation and absolute nodal coordinate formulation. In: Proceedings of the ASME 2007 International Design Engineering Technical Conferences & Computers and Information in Engineering Conference IDETC/CIE 2007; 2007. p. 12. doi:10.1115/DETC2007-34754.

[23] Argyris JH, Fried I, Scharpf DW. The TUBA family of plate elements for the matrix displacement method. Aeronaut J 1968;72(692):701–9. https://doi.org/10.1017/S000192400008489X.

[24] Ivannikov V, Tiago C, Pimenta PM. Generalization of the C1 TUBA plate finite elements to the geometrically exact Kirchhoff-Love shell model. Comput Methods Appl Mech Eng 2015;294:210–44. https://doi.org/10.1016/j.cma.2015.05.018.

[25] Kiendl J, Bletzinger K-U, Linhard J, Wüchner R. Isogeometric shell analysis with Kirchhoff-Love elements. Comput Methods Appl Mech Eng 2009;198(49–52):3902–14. https://doi.org/10.1016/j.cma.2009.08.013.

[26] Cirak F, Ortiz M. Fully C1-conforming subdivision elements for finite deformation thin-shell analysis. Int J Numer Meth Eng 2001;51:813–33. https://doi.org/10.1002/nme.182.

[27] Timoshenko S, Woinowsky-Krieger S. Theory of plates and shells. McGraw Hill; 1959.

[28] Vetyukov Y, Kuzin A, Krommer M. Asymptotic splitting in the three-dimensional problem of elasticity for non-homogeneous piezoelectric plates. Int J Solids Struct 2011;48(1):12–23. https://doi.org/10.1016/j.ijsolstr.2010.09.001.

[29] Eliseev V, Vetyukov Y. Theory of shells as a product of analytical technologies in elastic body mechanics. In: Pietraszkiewicz W, Górski J, editors. Shell Structures: Theory and Applications. CRC Press/ Balkema, Vol. 3. London: Taylor & Francis Group; 2014. p. 81–4.

[30] Naghdi P, Vongsarnpigoon L. A theory of shells with small strain accompanied by moderate rotation. Arch Rational Mech Anal 1983;83(3):245–83. https://doi.org/10.1007/BF00251511.

[31] Clebsch A. Théorie de l'élasticité des corps solides, Dunod, 1883, translated into French by Barré de Saint-Venant.

[32] Timoshenko S, Gere J. Theory of Elastic Stability, 2nd Edition, McGraw-Hill, New-York; 1961, Ch. 5. p. 212–250.

[33] Anderson R, Irons B, Zienkiewicz O. Vibration and stability of plates using finite elements. Int J Solids Struct 1968;4(10):1031–55. https://doi.org/10.1016/0020-7683(68)90021-8.

[34] De Borst R, Crisfield MA, Remmers JJ, Verhoosel CV. Nonlinear finite element analysis of solids and structures. John Wiley & Sons; 2012.

[35] Joulaian M, Düster A. Local enrichment of the finite cell method for problems with material interfaces. Comput Mech 2013;52:741–62. https://doi.org/10.1007/s00466-013-0853-8.

[36] Joulaian M, Hubrich S, Düster A. Numerical integration of discontinuities on arbitrary domains based on moment fitting. Comput Mech 2016;57:979–99. https://doi.org/10.1007/s00466-016-1273-3.

[37] Duczek S, Gabbert U. Efficient integration method for fictitious domain approaches. Comput Mech 2015;56(4):725–38. https://doi.org/10.1007/s00466-015-1197-3.

[38] Fries T-P, Omerović S. Higher-order accurate integration of implicit geometries. Int J Numer Meth Eng 2016;106:323–71. https://doi.org/10.1002/nme.5121.

[39] Kudela L, Zander N, Kollmannsberger S, Rank E. Smart octrees: Accurately integrating discontinuous functions in 3d. Comput Methods Appl Mech Eng 2016;306:406–26. https://doi.org/10.1016/j.cma.2016.04.006.

[40] Abedian A, Parvizian J, Düster A, Khademyzadeh H, Rank E. Performance of different integration schemes in facing discontinuities in the finite cell method. Int J Comput Methods 10; 2013. 24pp. doi:10.1142/s0219876213500023.

[41] Petö M, Duvigneau F, Eisenträger S. Enhanced numerical integration scheme based on image compression techniques: Application to fictitious domain methods. Adv Model Simul Eng Sci 2020;7(1):1–42. https://doi.org/10.1186/s40323-020-00157-2.

[42] Schillinger D, Cai Q, Mundani RP, Rank E. A Review of the Finite Cell Method for Nonlinear Structural Analysis of Complex CAD and Image-based Geometric Models, Springer Verlag; 2013, Ch. A Review of the Finite Cell Method for Nonlinear Structural Analysis of Complex CAD and Image-based Geometric Models, pp. 1–23. doi:10.1007/978-3-642-38762-3_1.

[43] Schillinger D, Ruess M. The finite cell method: A review in the context of high-order structural analysis of CAD and image-based geometric models. Arch Comput Methods Eng 2015;22:391–455. https://doi.org/10.1007/s11831-014-9115-y.

[44] Dauge M, Düster A, Rank E. Theoretical and numerical investigation of the finite cell method. J Sci Comput 2015;65:1039–64. https://doi.org/10.1007/s10915-015-9997-3.

[45] Hughes TJ, Cottrell JA, Bazilevs Y. Isogeometric analysis: CAD, finite elements. NURBS, exact geometry and mesh refinement. Comput Methods Appl Mech Eng 2005;194(39):4135–95. https://doi.org/10.1016/j.cma.2004.10.008.

[46] Cottrell J, Reali A, Bazilevs Y, Hughes T. Isogeometric analysis of structural vibrations. Comput Methods Appl Mech Eng 2006;195:5257–96. https://doi.org/10.1016/j.cma.2005.09.027.

[47] Kiendl J, Hsu M-C, Wu MCH, Reali A. Isogeometric Kirchhoff-Love shell formulations for general hyperelastic materials. Comput Methods Appl Mech Eng 2015;291:280–303. https://doi.org/10.1016/j.cma.2015.03.010.

[48] Kim HJ, Seo YD, Youn SK. Isogeometric analysis with trimming technique for problems of arbitrary complex topology. Comput Methods Appl Mech Eng 2010;199(45–48):2796–812.

[49] Breitenberger M, Apostolatos A, Philipp B, Wüchner R, Bletzinger KU. Analysis in computer aided design: Nonlinear isogeometric B-Rep analysis of shell structures. Comput Methods Appl Mech Eng 2015;284:401–57.

[50] Beer G, Marussig B, Zechner J. A simple approach to the numerical simulation with trimmed CAD surfaces. Comput Methods Appl Mech Eng 2015;285:776–90. https://doi.org/10.1016/j.cma.2014.12.010.

[51] Guo Y, Do H, Ruess M. Isogeometric stability analysis of thin shells: From simple geometries to engineering models. Int J Numer Meth Eng 2019;118(8):433–58. https://doi.org/10.1002/nme.6020.

[52] Kiendl J, Bazilevs Y, Hsu M-C, Wüchner R, Bletzinger K-U. The bending strip method for isogeometric analysis of Kirchhoff-Love shell structures comprised of multiple patches. Comput Methods Appl Mech Eng 2010;199:2403–16. https://doi.org/10.1016/j.cma.2010.03.029.

[53] Herrema AJ, Johnson EL, Proserpio D, Wu MCH, Kiendl J, Hsu M-C. Penalty coupling of non-matching isogeometric Kirchhoff-Love shell patches with application to composite wind turbine blades. Comput Methods Appl Mech Eng 2019;346:810–40. https://doi.org/10.1016/j.cma.2018.08.038.

[54] Guo Y, Ruess M. Nitsche's method for a coupling of isogeometric thin shells and blended shell structures. Comput Methods Appl Mech Eng 2015;284:881–905. https://doi.org/10.1016/j.cma.2014.11.014.

[55] Brivadis E, Buffa A, Wohlmuth B, Wunderlich L. Isogeometric mortar methods. Comput Methods Appl Mech Eng 2015;284:292–319. https://doi.org/10.1016/j.cma.2014.09.012.

[56] Horger T, Reali A, Wohlmuth B, Wunderlich L. A hybrid isogeometric approach on multi-patches with applications to kirchhoff plates and eigenvalue problems. Comput Methods Appl Mech Eng 2019;348:396–408. https://doi.org/10.1016/j.cma.2018.12.038.

[57] Chow FY, Narayanan R. Buckling of plates containing openings. In: Proceedings of the 7th International Specialty Conference on Cold-Formed Steel Structures; 1984. p. 39–53.

[58] Ruess M, Schillinger D, Bazilevs Y, Varduhn V, Rank E. Weakly enforced essential boundary conditions for NURBS-embedded and trimmed NURBS geometries on the basis of the finite cell method. Int J Numer Meth Eng 2013;95:811–46. https://doi.org/10.1002/nme.4522.

[59] Kollmannsberger S, Özcan A, Baiges J, Ruess M, Rank E, Reali A. Parameter-free, weak imposition of Dirichlet boundary conditions and coupling of trimmed and non-conforming patches. Int J Numer Meth Eng 2015;101:670–99. https://doi.org/10.1002/nme.4817.

[60] de Prenter F, Lehrenfeld C, Massing A. A note on the penalty parameter in Nitsche's method for unfitted boundary value problems. Comput Math Appl 2018;75(12):4322–36. https://doi.org/10.1016/j.camwa.2018.03.032.

[61] Sukumar N, Chopp DL, Moës N, Belytschko T. Modeling holes and inclusions by level sets in the extended finite-element method. Comput Methods Appl Mech Eng 2001;190:6183–200. https://doi.org/10.1016/s0045-7825(01)00215-8.

[62] Rees DWA. Plate Buckling Under Uniaxial Compression, John Wiley & Sons Ltd; 2009, Ch. Appendix B, pp. 525–535. doi: 10.1002/9780470749784.app2.

[63] Rees DWA. Plate Buckling Under Biaxial Compression and Shear, John Wiley & Sons Ltd; 2009, Ch. Appendix C, pp. 537–541. doi: 10.1002/9780470749784.app3.

[64] Buckling of flat plates in shear, Standard, Engineering Sciences Data Unit, Denver, USA; Feb. 1971.

[65] Savitzky A, Golay MJE. Smoothing and differentiation of data by simplified least squares procedures. Anal Chem 1964;36:1627–39. https://doi.org/10.1021/ac60214a047.

[66] Scheidl J, Vetyukov Y, Schmidrathner C, Schulmeister K, Proschek M. Mixed Eulerian-Lagrangian shell model for lateral run-off in a steel belt drive and its experimental validation. Int J Mech Sci 2021:106572. https://doi.org/10.1016/j.ijmecsci.2021.106572.